ANALYSIS OF THE AEROACOUSTIC PERFORMANCE OF TWIN PROPELLERS IN HOVER BY USING THE CIRA-CUSANO TEST RIG

Antonio Visingardi, Mattia Barbarino, Fabrizio De Gregorio
CIRA, Capua, Italy
Luca Greco, Claudio Testa, Stefano Zaghi
CNR, Rome, Italy
Jianping Yin
DLR, Braunschweig, Germany
Gabriel Reboul
ONERA, France
Andrea Cavalli, Daniele Granata, Luca Abergo, Alberto Guardone, Alex Zanotti
Politecnico di Milano, Dipartimento di Scienze e Tecnologie Aerospaziali, Milan, Italy
Giovanni Bernardini, Caterina Poggi
Roma Tre University, Rome, Italy
Paolo Candeloro, Tiziano Pagliaroli
University Niccolò Cusano, Rome, Italy
George Barakos, Geng Qiao
University of Glasgow, United Kingdom
Florian Fausel, Manuel Keßler, Moritz Muth
University of Stuttgart, Germany

Abstract

The present work illustrates numerical-experimental aeroacoustic investigations of single and twin co-rotating propeller configurations in hover flight. The activity was aimed at evaluating the effect of the inter-axis distance between the twin-propellers, the phase angle, and the sense of rotation of the secondary propeller, with respect to the main one, on the aeroacoustic properties of the examined configurations. Loads, PIV, and microphone measurements were jointly conducted by CIRA and Cusano University at CIRA. Specifically, aerodynamic and fluid dynamic measurements were performed in a laboratory environment, while acoustic measurements were conducted in a semi-anechoic chamber. The aerodynamic simulations were carried out by using solvers of different degrees of fidelity, from panel methods to URANS solvers, whereas the aeroacoustic analyses were all based on the Ffowcs Williams-Hawkings formulation. Both numerical and experimental results show that the loads acting on each propeller reduce passing from the single propeller to the twin-propeller configuration. This reduction decreases as the distance between the propellers increases. Negligible effects are produced on the loads by changing the phase angle and the sense of rotation of the secondary propeller. Conversely, the acoustics is more sensitive to these configurational changes: the noise produced by the twin propellers is higher than that of the single propeller, and the maximum is reached at the lower separation distance between the two propellers. De-phasing or changing the sense of rotation of the secondary propeller produces the highest increase in noise, with the maximum reached at the phase angle $\Delta\varphi = 60°$.

1. NOTATION

Symbols

c	Blade chord, m
CQ	Propeller torque: $Q/\rho n^2 D^5$

CT	Propeller thrust: $T/\rho n^2 D^4$
D	Propeller diameter, m
n	Propeller speed, 1/s
Q	Propeller torque, Nm
R	Propeller radius, m
SPL	Sound Pressure Level, dB
T	Propeller thrust, N
T_{hk}	Blade thickness, m
u, v, w	Induced velocity components in the PIV planes, m/s
x, y, z	Coordinates of the PIV planes, m
P_i	Induced power, kW
β	Blade pitch, deg
$\Delta\varphi$	Phase angle between the main blades of the two propellers, deg
ρ	Air density, kg/m^3
σ	Propeller solidity
ψ	Azimuth angle, deg
ω, Ω	Propeller speed, RPM

Acronyms:

BEM	Boundary Element Method
BPF	Blade Passage Frequency
eVTOL	electric Vertical Take-off and Landing
FWH	Ffowcs Williams-Hawkings
PIV	Particle Image Velocimetry
UAM	Urban Air Mobility
URANS	Unsteady Reynolds-Averaged Navier Stokes

2. INTRODUCTION

The use of multirotor eVTOL aircraft is the key point for the successful implementation of UAM, an “air transportation system for passengers and cargo in and around urban environments” (EASA definition).

However, the noise generated by these aircraft can have a highly detrimental impact on the sustainability and social acceptability of this novel system. In particular, surveys conducted by EASA on the societal acceptability of UAM in Europe, Ref.1, regard noise as the highest concern of respondents when UAM aircraft are used for air taxi operations. For this reason, the aeroacoustics of multirotor configurations is a topic that is gaining ever increasing interest in the aviation research community.

The design of low-noise multirotor aircraft is a relatively new topic of research which requires an in-depth understanding of the physics related to noise sources, especially multiple interactions and near-field sound propagation. Compared to conventional helicopters, the importance of the various noise sources and the influence of the noise scattering can be different. In addition, the ranges of the flow regimes are substantially different: helicopters typically fly at Reynolds numbers O(10^6) whereas multirotor eVTOLs, which are equipped with blades of smaller sizes, fly at Reynolds numbers O(10^4 – 10^5). The main noise sources for conventional helicopters are well known, for example blade vortex interaction noise (BVI) in descent flight, but by using distributed single or co-axial rotors, the multiple interactions among rotors and the rotor-wake interactions may play an important role in the total noise signal. Ducts, wings or the fuselage may also shield or scatter the noise during its propagation. In addition, broadband noise may become a dominant noise source for rotors with low tip Mach number or disturbed rotor inflow.

A basic understanding of the interactional aerodynamics and acoustics of multirotor configurations can be made by considering a pair of rotors placed side-by-side or in tandem configuration. Many experimental and numerical investigations have been published in recent years related to such simplified configurations:

Zhou et al., Ref.2, studied the impact produced by interactions of side-by-side rotors on the aerodynamic and aeroacoustic performances of small UAVs using load cells, microphones, and the Particle Image Velocimetry (PIV) experimental technique. They explored different distances between the rotors and observed that, while the separation distance had a very limited effect on the thrust coefficient of the rotor (i.e., variation within 2% for all test cases), the thrust fluctuations (i.e., thrust standard deviation) were found to increase dramatically as the separation distance becomes smaller. Similarly, a maximum noise enhancement of ~3 dB was observed for the L = 0.05D case in comparison to that of the L = 1.0D case, which was the result of both tonal and broadband noise.

Shukla and Komerath, Ref. 3, carried out high-speed (400 Hz) Stereo PIV and performance measurements for two counter-rotating rotors placed side-by-side at different distances. The interaction became prominent for the closest configuration with a degradation of the aerodynamic performances. The instantaneous flow field measurements indicated high inter-rotor wake interactions for small axis shifts causing rotor wake features to distort, lose coherence and deviate from their typical trajectories.

Ko et al., Ref. 4, performed numerical aeroacoustic simulations based on the free wake vortex lattice method and FWH solver for the identification of the wake interactional effects acting on the DJI F450 quadcopter drone in hover and forward flight. They found that the spacing between the rotors in hovering flight significantly affected the aerodynamic and aeroacoustic characteristics where the unsteady loading of multirotor changed periodically and the loading fluctuation increased by decreasing the spacing. It also caused variations in the unsteady loading noise and noise directivity patterns.

Bu et al., Ref. 5, conducted aerodynamic and acoustic tests of two coplanar small-scale propellers in an anechoic chamber. The experimental measurement showed that the interactional effects of the dual propellers have little influence on the mean thrust, and the tonal noise at the BPF and the OASPL are little impacted at the higher observation angles away from the wake region. Instead, it was observed that the tones at the high BPF harmonics are noticeably affected, due to the sensitivity to the unsteady aerodynamic loading on the blades.

Stokkermans et al., Ref. 6, studied the wake interaction of two propellers in two different orientations: side-by-side and one after another, with respect to the flow direction of the wind tunnel. They pointed out that the wake interaction strongly depends on the arrangement of the rotors with penalties in power when compensating for the thrust loss. Similar observations were outlined by Zanotti et al., Ref. 7 , for two propellers arranged in such a manner that their wakes overlap each other in wind tunnel tests. They argued that a partial overlap of propeller wakes determines acoustic drawbacks, as well as detrimental effects on aerodynamic performances.

Zarri et al., Ref. 8, investigated tip-on-tip and tip-on-strut interactions of a commercial drone in hover by applying a hybrid methodology combining URANS simulations with FWH aeroacoustics approach. They found that the tip-on-tip interaction, without fuselage, reduced the average thrust of each propeller by 7%, while increasing its fluctuations by 7% compared to the isolated case. The reason for this was attributed to the sudden breakdown of the coherent vortical structures that were instead observed to develop downstream of the propeller alone. The interaction with the supporting struts induced additional periodic loads on the blades at multiples of the blade passing frequency. The sound directivity maps in the near field were found to be relevantly altered, up to 30 dB differences, when comparing the sound emission including or not the drone body.

In the framework of the Rotorcraft (RC) Group of Responsables of the European GARTEUR initiative, Ref. 9, two action groups were launched to investigate the rotor-rotor interactional aerodynamics, RC/AG-25 “Rotor - Rotor Wakes Interactions”, Ref. 10; and the aeroacoustics of multi-rotor configurations, RC/AG-26 “Noise Radiation and Propagation for Multirotor System Configurations”, Ref. 11. Numerical and experimental investigations were carried out by the consortium of RC/AG-25 on a quadcopter model, without fuselage, to evaluate the effects of the layout (square, bearhug and breaststroke) and the mutual distance of the four propellers, mainly in terms of aerodynamic performance but the aeroacoustic behaviour was also studied. In particular, the aerodynamic analyses, Ref. 12, indicated that the efficiency of a diamond configuration improves by 5% in comparison with isolated rotors for non-overlapping rotor spacings, while the interactions in square alignments are detrimental for all analysed test cases with the optimum at 0.04D blade overlap. The trend was found to be more pronounced for the backward rotor tilt with intensified interactions, for which the efficiency of the diamond configuration increased by 11% at 1.2D rotor spacing. The aeroacoustic analyses, Ref. 13, indicated that, even though noise levels increase with reducing rotor separation, the choice of the rotor phasing has a greater influence with orthogonal phasing at 1.2D producing 6 dB less noise for the square configuration. The diamond configuration with 1.2D rotor spacing and tip-to-tip phasing was shown to be the most beneficial both aerodynamically and acoustically for analysed observers.

Concerning the RC/AG-26, CIRA and Univ. Cusano carried out an experimental activity in the semi-anechoic test chamber of CIRA for an isolated and twin-propeller test rig in hover, at different speeds and mutual radial distances. The outcomes of this activity, illustrated in Ref. 14, indicated that the aerodynamic loads on each rotor in a side-by-side configuration exhibited thrust and torque reductions in comparison to the single propeller. The interaction due to the propeller vicinity reduced the thrust by about 5.5% and the torque by about 9.5%. In addition, an increment in the load fluctuations was observed by reducing the radial distance of the two propellers. The aeroacoustic measurements highlighted a higher level of noise of about 12% in the side-by-side configuration, particularly in the inlet flow and side zones in the ranges [180°; 220°] and [310°; 350°].

Furthermore, a joint test program for aerodynamic and acoustic measurements was conducted by DLR and CIRA. The acoustics experiments were carried out in the DLR's Acoustic Wind Tunnel Braunschweig (AWB), while the PIV measurements were conducted at CIRA. Configurations in isolated, tandem and co-axial configurations were tested. Both aerodynamic and aeroacoustic simulations indicated that measurement results in terms of rotor performance, flow field and acoustic signals for most cases were reproducible and the comparison of the simulations and the test gave satisfactory agreement by all computational methods, regardless of their fidelity level, Ref. 15.

The present paper illustrates the outcomes of the numerical comparisons carried out by the authors with the experimental database, produced by CIRA and the University Niccolò Cusano, on the isolated and twin propeller configurations described in Ref. 14.

3. DESCRIPTION OF THE ACOUSTIC AND PIV SET-UP

3.1. Rotor rig

A specific setup was designed to characterize the acoustic signature of a multirotor drone. The tests were performed in a semi-anechoic chamber at the Italian Aerospace Research Centre (CIRA), Figure 1, to eliminate background noise interference. The chamber has dimensions of $5.65\,m\,x\,4.45\,m\,x\,4\,m$ and a cut-off frequency of $90\,Hz$. The Univ. Cusano Rotor rig consists of two KDE-CF155-TP 115.5x5.3 three-bladed propellers characterized by a diameter $D = 393.7\,mm$ and a medium chord $c = 28.5\,mm$. The resulting rotor solidity value is equal to $\sigma = 0.138$.

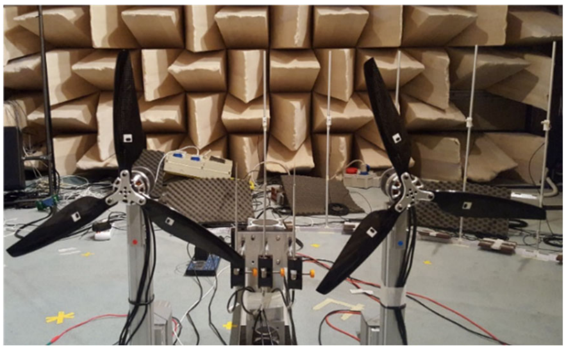

Figure 1: Rotor rig set-up in the CIRA semi anechoic test chamber

The propeller blade geometry is reported in Figure 2 in terms of radial distributions of chord c, thickness T_{hk}, and blade pitch β.

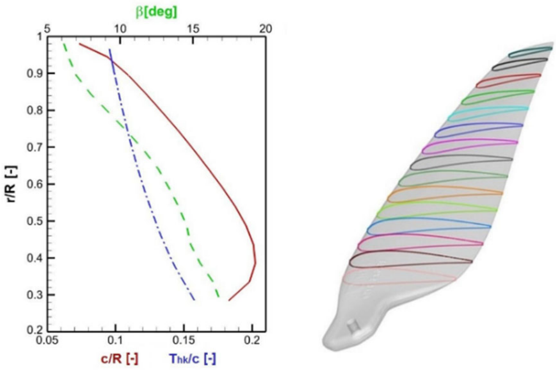

Figure 2: KDE-CF155-TP Propeller geometry

The propellers were driven by two brushless motors type KDE4012XF-400 connected to a dedicated electronic speed controller (ESC) model KDEXF-UAS55. A custom system was implemented to control the propellers rotational speed using an NI PXI-1031 with motion controller NI-PXI-7350 and multifunction DAQ NI PXI-6259.

The speed of the propellers and the relative position of the blades were measured by means of a Kubler 05.2400 incremental encoder with 500 pulses per revolution (PPR). The propellers, motors, and encoder were mounted on a specific vertical aluminium support structure. In order to investigate the effect of the phase control between the two propellers on the pressure field, a synchrophaser was designed and implemented in the LabVIEW programming environment. The relative phase angle ψ between the two propellers is defined in Figure 3.

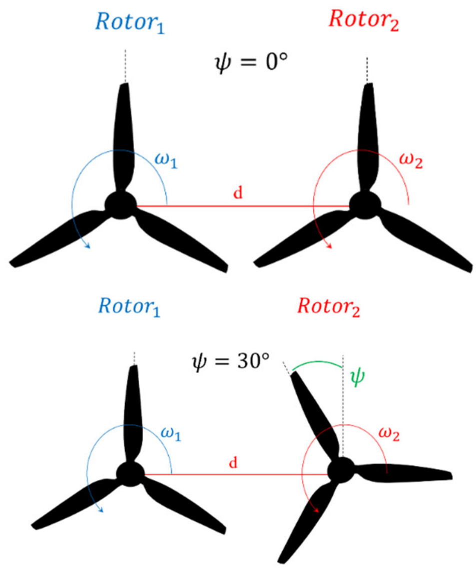

Figure 3: Definition of the sense of rotation and phase angle between the propellers.

To measure the propeller aerodynamic loads, the Kubler encoders were removed and the motors were fixed to the ATI Mini 40 balance. The measurements were carried out at a sampling frequency of 1000 Hz for a time of 20 seconds. Mean force and moments were evaluated together with the standard deviation. The resulting rotor rig configuration is shown in Figure 4. Only the loads of the main rotor, rotor#1, were measured, the secondary rotor, rotor#2, was mounted on a dummy balance to preserve the symmetry of the rotor rig. Since the encoder was removed, the rotational speed was measured using a single microphone positioned in close proximity to rotor#1.

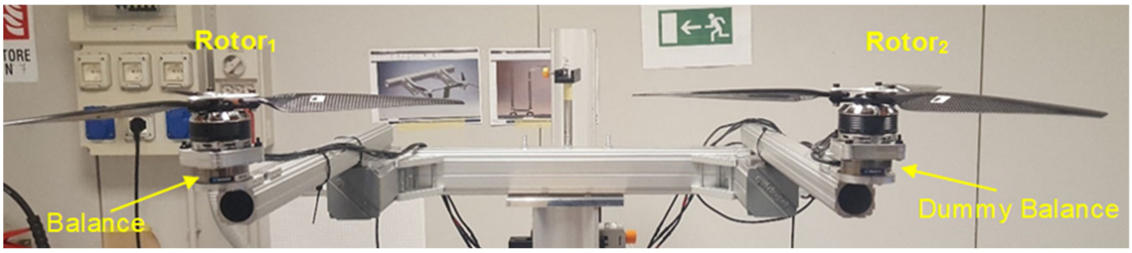

Figure 4: Rotor rig equipped with 6 components load cells

3.2. Acoustic set-up

The far field acoustic measurements were carried out using a moving microphone circular array consisting of eight G.R.A.S. 40PK CCP microphones and spanning the entire circumference, with an angular resolution of 10°. A sketch of the setup employed is shown in Figure 5.

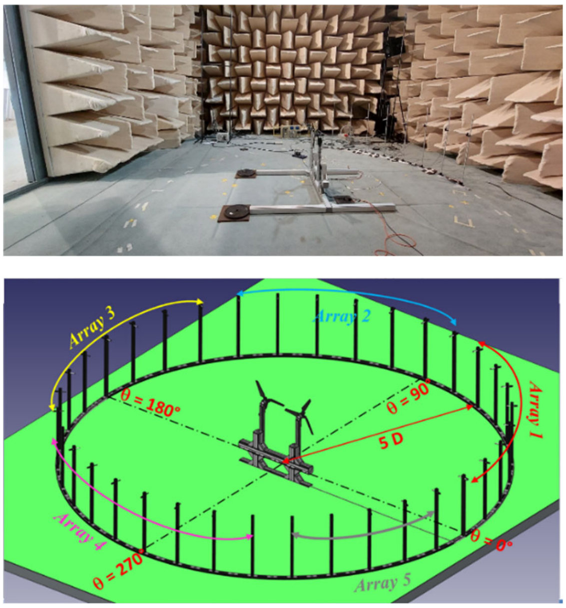

Figure 5: Experimental setup inside the semi-anechoic chamber (top) and circumferential arrangement of microphones with the polar angle Θ definition (bottom)

The microphones were positioned at a distance of 5D from the midpoint between the two rotors. Each microphone is characterized by a frequency range from 20 to 20000 Hz and a dynamic range from 26 to 145 dB(A). The pressure time histories were acquired using a National Instruments NI cDAQ-9174 data acquisition board with a sampling frequency of 12800 Hz and an acquisition time of 30 s.

The experimental tests were performed at two rotational speeds: $\Omega_1 = 5200RPM$ and $\Omega_2 = 3500RPM$ considering three values for the rotors mutual distance: d=1.02D, d=1.1D, and d=1.2D, respectively. The effect of reversing the sense of rotation of the secondary propeller was tested in some cases. The phase angle between the propellers varied in the range of $\psi = 0^{\circ} - 105^{\circ}$. In addition to these test cases, two additional configurations for the phase shift were considered, referred to as "random", where the slave motor follows the master motor by oscillating around an equilibrium value with a sinusoidal law and a fixed maximum amplitude of 10°.

3.3. PIV experimental layout

The rotor downwash characteristics were measured by two-component Particle Image Velocimetry (2C-PIV) measurement systems. The set-up was composed of a CFR 400 dual-head Nd-Yag laser with a pulse energy of 180 mJ at a wavelength of 532 nm and a repetition rate of 10 Hz. A system of two sCMOS cameras was installed consisting of two ILA.PIV.sCMOS CLHS. The cameras were installed on a two-axis linear traversing system, to increase the measured region by horizontally shifting the cameras. The investigation of both the isolated propeller and the tandem configurations drove the installation of the two cameras side-by-side and vertically aligned to follow the wake evolution along the axial direction down to more than one rotor diameter, Figure 6. For the isolated propeller, the measured region of interest covered radially the wake in the range between $x = 0.23\ R$ to $x = 1.17\ R$ and vertically from $z = 0.1\ R$ to $z = -2.05\ R$, while for the tandem configuration, a larger region is recorded ranging between $x = 0.5\ R$ and $x = 1.75\ R$ along the x-direction and in the range comprised from $z = 0.09\ R$ to $z = -2.06\ R$ in the vertical direction. As tracer particles, aerosolized diethylhexylsebacate (DEHS) oil with a size of less than 1 μm was used. The PIV images were pre-processed by applying a background grey-level subtraction. PivView v3.6.5 (by PivTech GmbH) was used to process the particle images. The particle image analysis consisted of an iterative multigrid cross–correlation algorithm. The results presented a vector step of $\Delta x = 1.43\ mm$. Considering the current values for the optical resolution (11.21 px/mm) and the laser double–pulse delay (45-60 μs), a velocity error εu of ~ 0.2 m/s to 0.15 m/s was estimated. A complete description of the measurement setup and a discussion of the preliminary experimental results were given by De Gregorio et al. in Ref. 16.

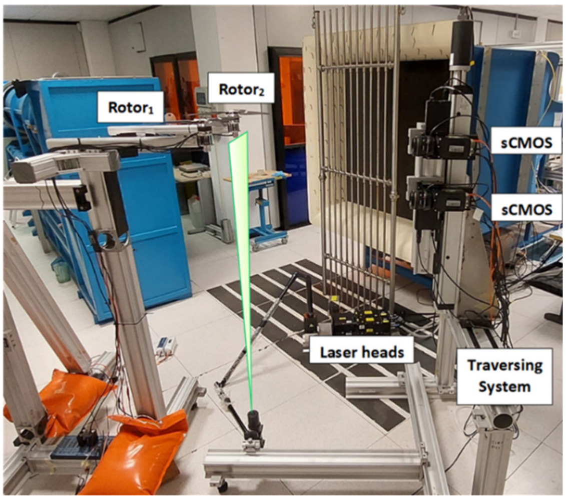

Figure 6: Experimental Layouts: 2C-PIV

4. DESCRIPTION OF THE METHODOLOGIES FOR THE NUMERICAL SIMULATIONS

The numerical simulations were performed by the partner applying in-house-developed and commercial computational tools, of different degrees of fidelity, and validated through comparisons with the experimental data produced during the AG-26 project. The list of the numerical solvers is summarized in Table 1 and a detailed description is provided in the following.

Table 1: Main Characteristics of the codes used by the partners

Partner	Code	Description
CIRA	RAMSYS, ACO-suite	Unsteady, inviscid and incompressible free-wake Boundary Element Method (BEM) + Ffowcs Williams-Hawkings (FWH)
DLR	UPM, APSIM	Free Wake Panel method, FWH
ONERA	ProLB, KIM	Lattice Boltzmann Method (LBM), FWH
Politecnico Milano	DUST	Free Wake Panel method, FWH
Roma Tre Univ. / CNR	AERMOD, ACUMOD	Unsteady, inviscid and incompressible free-wake BEM + FWH
Univ. Stuttgart	FLOWer, ACCO	FLOWer: unsteady, compressible (URANS) CFD solver with Chimera technique, FWH Solver with source-time dominant algorithm
Univ. Glasgow	HMB3-HFWH	HM3 CFD solver, unsteady, compressible (URANS), overset/chimera grids, FWH coupled with HMB3

4.1. CIRA

The CIRA aerodynamic simulations were carried out by using the medium-fidelity code RAMSYS, Ref. 17, which is an unsteady, inviscid and incompressible free-wake vortex lattice boundary element methodology (BEM) solver for multi-rotor, multi-body configurations developed at CIRA. It is based on Morino's boundary integral formulation, Ref. 18 for the solution of Laplace's equation for the velocity potential φ. The surface pressure distributions are evaluated by applying the unsteady version of Bernoulli equation, which is then integrated to provide the forces and moments on the configuration and the surrounding obstacles. A computational acceleration is obtained by applying the module for symmetrical flows and geometries implemented in the solver and the parallel execution via the OpenMP API. The pylons supporting the propellers were modelled as cylinders of square section.

The ACO-FWH solver is used for computing the acoustic free-field generated by the rotor blades. It is based on the FWH formulation, Ref. 19, described in Refs. 20, 21 and 22. The advanced-time formulation of Farassat 1A, Ref. 23, is employed, and the linear terms (the so-called thickness and loading noise contributions) are computed through integrals on the moving blades' surface (impermeable/rigid surface formulation). The computational acceleration is obtained by a parallel execution via the MPI API. The simulation of the aeroacoustic free-field was carried out by using the aerodynamic database evaluated by RAMSYS, and consisting of the rotor blade pressure distributions.

4.2. DLR

The free-wake panel method UPM, Refs. 24, 25, 26 is based on a velocity-based, indirect potential formulation using a combination of source and vortex distribution on the solid surfaces and vortex panels in the wake. Compressibility effect of the flow are considered by applying the Prandtl-Glauert correction. An iterative pressure Kutta condition is implemented to subsequently ensure pressure equality at the trailing edge. This method is proved to be computationally efficient and robust with respect to the size of the chosen time step and the number of panels on the blade. The pressure on the blade surface is calculated from the unsteady Bernoulli equation. The BVI is captured thanks to the free wake model used in UPM. The wake can also be represented in the form of vortex particles as UPM is linked to a particle solver. Depending on the configurations, all aerodynamic interactions are considered.

The Aeroacoustic Prediction System based on an Integral Method, APSIM, Ref. 27, is designed to calculate wave propagation over large distances in uniform flows. The methodology is based on FWH formulation, Ref. 19, and only linear sound propagation is considered. In general, the aeroacoustic computation into the far field is split into two steps for current applications: In a first step the pressure data on the rotor is computed by aerodynamic codes and provided to APSIM; in a second step the sound propagation into the far field is calculated with APSIM. Validations of UPM and APSIM were intensively conducted during various projects.

4.3. ONERA

Simulations using the Lattice Boltzmann Method (LBM) are performed with the ProLB code, Ref. 28. The ProLB solver is developed in the framework of a French consortium composed of universities, and industries. For 3-D applications, the code is based on a 19-velocity discretization (D3Q19 lattice) with no additional equations or distribution functions. Consequently, the version of the code used v2.8) is limited to isothermal or weakly compressible flows. In practice, the lattice Boltzmann equation is solved on non-body fitted grids based on a hierarchy of embedded cartesian grids with a ratio of 2 between the grid spacing of two successive refinement levels (Octree approach), combined with an unstructured topology. This strategy allows for an easy meshing of complex geometry but special care must be taken to ensure smooth transitions between refinement levels. To do so, the collision operator used in this study is the Hybrid Recursive Regularized (HRR) model presented in Jacob et al., Ref. 29, and the Direct Coupling approach proposed by Astoul et al., Ref. 30, is also considered. A turbulence model is adopted to avoid the prohibitive cost of direct numerical simulations. The shear improved Smagorinsky model of Leveque et al., Ref. 31, is chosen here.

The longitudinal extension of the computational domain is equal to 30 times the radius of the propeller, combined with non-reflecting boundary conditions ensures the absence of aerodynamic or acoustic reflections. The total number of points is equal to 145 million with one propeller and 261 million for the tandem configuration. An additional refinement has been added at propellers tips in order to allow small separation distances. Even if the code uses a wall law, the smallest cell size on the propeller is set equal to 0.14 mm (0.5% of tip chord) to ensure that y+ values are small enough on the blades (less than 60). Since the time scheme is explicit (CFL=1), it implies tiny time steps, in this case 0.24 μs. To ensure statistical convergence the simulation is run over 16 revolutions over which the last 9 are used for acoustic post-processing.

The unsteady surface pressure distribution on the blades obtained with ProLB are used as input for the KIM code, Refs. 32 and 33, to determine the noise emission of the rotor thanks to a Ffowcs-Williams and Hawkings formulation implemented in a non-compact advanced time approach.

Once the acoustic pressure signals are obtained a phase averaging is employed in order to decompose the signals into periodic (tonal noise) and non-deterministic parts (broadband noise). It is then possible to determine the noise directivities at specific frequency tones.

4.4. Politecnico di Milano (PoliMi)

The single and twin propeller test cases were simulated by the mid-fidelity DUST solver, Ref. 34. DUST is an open-source software developed by PoliMi to simulate the interactional aerodynamics of unconventional rotorcraft configurations. The code, released as free software under the open-source MIT license, relies on an integral boundary element formulation of the aerodynamic problem and a vortex particle model of the wakes. The propeller blades were modelled using surface panels elements, thus without using viscosity corrections. In particular, a number of 240 surface panels were used to model each blade, using a spanwise discretization of 15 panels and a chordwise discretisation of 8 panels. Simulations were performed using a time-discretization of 5° azimuthal angle for a total of 8 revolutions. The aerodynamic results obtained by are not trimmed. The aeroacoustic signature is computed by solving FWH equations, Ref. 19. The surface pressure field on the propeller computed with the two solvers is provided as input to the same acoustic module, Ref. 35. The support system of the propellers was not modelled.

4.5. Roma Tre University & CNR (RM3)

Under the framework of GARTEUR AG-26, Roma Tre University (RM3) and the National Research Council of Italy (CNR) are collaborating to advance their collective understanding of drone aeroacoustics. Aerodynamic and aeroacoustic solvers used by both research units are based on tools developed over the past twenty years, which have been extensively validated on helicopter and tiltrotor configurations, Refs. 36 and 37, marine/aeronautical configurations powered by rotating wings, Refs. 38, 39 and 40, and wind turbine applications, Ref. 41. For simplicity, all results presented in this paper are labelled as RM3.

The aerodynamic module is based on the boundary integral formulation for the velocity potential presented in Ref. 42 suited for helicopter configurations where blade-vortex interaction (BVI) occurs. This formulation is fully 3D, can be applied to bodies with arbitrary shape and motion, and allows the calculation of both wake distortion and blade pressure field. It assumes the potential field to be divided into an incident field, generated by doublets over the wake portion not in contact with the trailing edge (far wake), and a scattered field, generated by sources and doublets over the body as well as doublets over the wake portion very close to the trailing edge (near wake). This procedure allows one to overcome the instabilities arising when the wake comes too close to or impinges on the body. Recalling the equivalence between the surface distribution of doublets and vortices, the contribution of the wake portion experiencing BVI (far wake) is expressed in terms of thick vortex (i.e., Rankine vortices) distributions. The shape of the wake can be either assigned (prescribed-wake analysis) or obtained as a part of the solution (free-wake analysis) by a time- marching integration scheme in which the wake is moved accordingly to the velocity field computed from the potential solution. Once the potential field is known, the Bernoulli theorem yields the pressure distribution on the body that, in turn, is used both to determine the aerodynamic loads and as an input to the aeroacoustic solver to predict the radiated noise. The aeroacoustic analysis is performed by a prediction tool based on FWH equation, Ref. 19. The solution of the FWH equation is achieved through the boundary integral representation known as the Farassat Formulation 1A, Ref. 23.

4.6. University of Glasgow (UoG)

Helicopter Multi-Block (HMB3) code is employed in this study. The solver can accurately predict the aerodynamic performance and acoustics of rotors, and has been widely used in the investigation of rotorcraft flows, Ref. 43, and helicopter rotor aeroelasticity, Ref. 44. Moreover, a good agreement when compared to experimental results in aerodynamics, acoustics and aeroelasticity of propellers, can be seen in a previous study, Ref. 45. Most recently, its ability to capture the interactions of multi-rotor flows and ducted propeller flows was documented by Qiao in Ref. 46 and Ref. 47. HMB3 solves the Unsteady Reynolds Averaged Navier-Stokes equation in integral form using the Arbitrary Lagrangian-Eulerian formulation for time-dependent domains, including moving boundary layers. HMB3 uses a cell-centred finite volume approach to discrete Navier-Stokes equations on multi-block, structured grids. The 3rd-order MUSCL (Monotone Upstream-centred Schemes for Conservation Laws) approach is applied to provide high-order accuracy in space. In the present work, simulations are performed with the $k-\omega$ shear stress transport (SST), Ref. 48, turbulence model.

The computational grids used for propellers have a typical C-H topology. The spacing distribution has been set to the condition $y^+ \leq 1$, resulting in a first cell size normal to the surfaces of approximately $1.0 \times 10^{-5}c$ as tested a-posteriori. Adiabatic, non-slip, wall boundary conditions were applied at propellers.

Regarding acoustics, the present work estimates the near-field information derived from pressure fields computed with the high-fidelity HMB3 tool. The sound pressure signal was obtained by subtracting the time-averaged pressure from the time-dependent data. Near-field CFD grids are designed to have at least 20 cells per target wavelength, which is calculated based on 20 times the Blade Passing Frequency (BPF = 260 Hz), Refs. 15 and 49.

The coupling of HMB3-HFWH tools was applied with the input of surface pressure fields computed by HMB3 to efficiently calculate the far-field acoustics. Current work focuses on the non-porous formulation with a completely anechoic condition. Extensive code-to-code comparisons of the current acoustic solver have been validated by Smith, Ref. 50.

4.7. University of Stuttgart (IAG)

For high-fidelity simulations, a framework consisting of FLOWer and ACCO was used at the Institute of Aerodynamics and Gas Dynamics (IAG) at the University of Stuttgart. CFD results are obtained with the block-structured code FLOWer, originally developed by DLR, Ref. 51, and continuously extended at the IAG for rotorcraft and multirotor applications, Ref. 52. Acoustic coupling was provided by IAG's FWH solver ACCO, Ref. 53, which uses the transient flow data provided by FLOWer as an input.

FLOWer solves the three-dimensional, compressible RANS equations and enables unsteady flow solutions (URANS). The discretization of time and space is applied separately by the method of lines. For temporal discretization a second-order dual time stepping is used, Ref. 54, with a time step of 0.5° to resolve acoustic waves, while for spatial discretization a 5th high-order weighted essentially non-oscillatory (WENO) scheme by Borges, Ref. 55, is used. Furthermore, the Menter-SST turbulence model was applied to close the URANS equations. Using the Chimera technique separate meshes were created for the background and rotor, utilizing hanging grid nodes to reduce the numerical expense. The spatial resolution of a single three-bladed rotor was achieved by 3.1 million cells. The rotor surface was meshed with 132 cells in radial and 40 cells in chordwise direction with a refinement towards the blade tip, leading edge and trailing edge with cell sizes of less than one thousandth of the radius. In addition, a hub region was constructed to connect the three rotor blades. The rotor mesh is extruded in wall normal direction with 56 cells. The first surface cells satisfy y+ < 1 and an extrusion up to cell sizes corresponding 10% of the chord length is applied. The spatial discretization in the background mesh was based on the resolution of the first harmonic wave length, with 15 cells discretizing the wave length of the BPF.

The acoustic code ACCO is an in-house code of the IAG, which uses an acoustic integration surface for the generation of sound emissions. For the integration either the physical surfaces or a permeable surface surrounding the object of interest can be used. For the performed simulations, the physical blade data of 5 full rotor revolutions are used and the integration is achieved through the physical surface of the rotor blade, which includes all tonal sound sources.

5. TEST CASES SELECTED FOR THE NUMERICAL SIMULATIONS

The test cases selected for the numerical simulations, Table 2, deal with an isolated propeller rotating counter-clockwise at $5200\ RPM$, and a set of twin counter-clockwise co-rotating propellers, also rotating at $5200\ RPM$, installed at the same height and at three different inter-axis distances: $d/D = 1.02$; 1.10 and 1.20, where D represents the propeller diameter. In addition, the effect of reversing the sense of rotation of the secondary propeller (CR) or de-phasing it with respect to the main one was also evaluated.

Table 2: Test cases selected for the numerical simulations

Test Nr.	d/D	Δφ [°]	Density [kg/m^3]	SoS [m/s]
Hov01 (SP)	-	-	1.198	344.75
Hov02 (TP)	1.02	0°	1.198	344.75
Hov03 (TP)	1.02	30°	1.198	344.75
Hov04 (TP)	1.02	90°	1.198	344.75
Hov11 (TP)	1.02	60°	1.222	343.23
Hov12 (TP)	1.10	0°	1.222	343.23
Hov14 (TP)	1.20	0°	1.222	343.23
Hov16 (TP)	1.02	CR	1.222	343.23

6. RESULTS OF THE NUMERICAL SIMULATIONS

6.1. Aerodynamic performance

Medium- and high-fidelity numerical simulations were carried out by using the discretization indicated in Table 3 and Table 4, respectively.

Table 3: Space and time discretization for the mediun fidelity aerodynamic simulations

Partner	Panels per Blade / Pylon	Azimuth step [°]	Revs / Wake spirals
CIRA	1320 / 2808	2	10 / 10
CNR	3400 / -	2	7 / 6
DLR	1624 / -	2	10 / 10
PoliMi	240 / -	5	8 / 8
RM3	6000 / -	3	10 / 6

Table 4: Space and time discretization for the CFD aerodynamic simulations

Partner	Grid cells Rotor / Total	Azimuth step [°]	Revs
IAG	3.1M / up to 18.7M	1 / 0.5	31
ONERA	- / up to 261M	0.011	16
UoG	7.5 / 38M	2	13

The aerodynamic performance of the single and twin propeller configurations was evaluated in terms of:

- Global loads, produced by each propeller. Namely, the time-averaged thrust and torque coefficients were measured and calculated;
- Time histories of the numerical thrust coefficient, for the whole configurations expressed as the summation of the CTs of the two propellers: $CT = CT_{Main} + CT_{Secondary}$. The CT of the single propeller was multiplied by 2 and chosen as reference value in order to have a more direct comparison with the twin propellers. This representation was selected with the aim to highlight the unsteadiness of the interactional aerodynamics of the single and twin-propellers in terms of n/rev frequency content and evaluate the effects on the propellers' noise.
- PIV measured and numerically simulated, to highlight the details of the flow field downstream of the propellers' disks, mainly in terms of the z-component of the induced velocity.

The analysis of the numerical-experimental comparisons is described in the following.

Time-averaged loads

Figure 7 illustrates the time-averaged thrust coefficient of the secondary propeller rotor#2 at several inter-axis distances between the twin propellers. All predictions show that this value is lower than the one produced by the single propeller, within 2.42% at $d/D = 1.02$, and that the closer the twin propellers are, the higher the reduction in thrust is. This behaviour is confirmed by the experiment, Ref. 14, which however shows a higher reduction, about 6% at $d/D = 1.02$. An explanation for this behaviour was identified by Shkula et al., Ref. 3, in the sudden breakdown of the coherent vortical structures that were instead observed to develop downstream of the single propeller. Figure 8 illustrates the loss of coherence in the wake structure produced by the propeller-propeller interactions.

By increasing the distance between the propellers' axes, the decrease in thrust reduces asymptotically. CIRA, PoliMi and RM3 show a lower reduction in thrust with respect to the single propeller, whereas the other simulations show a higher reduction with DLR and UoG results showing the highest value.

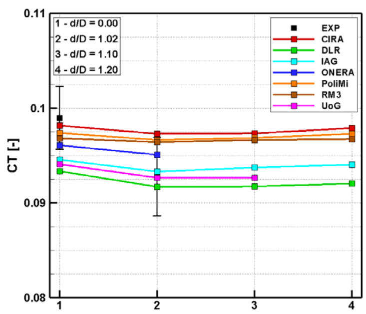

Figure 7: Thrust coefficient of the secondary propeller at several distances between the twin propellers

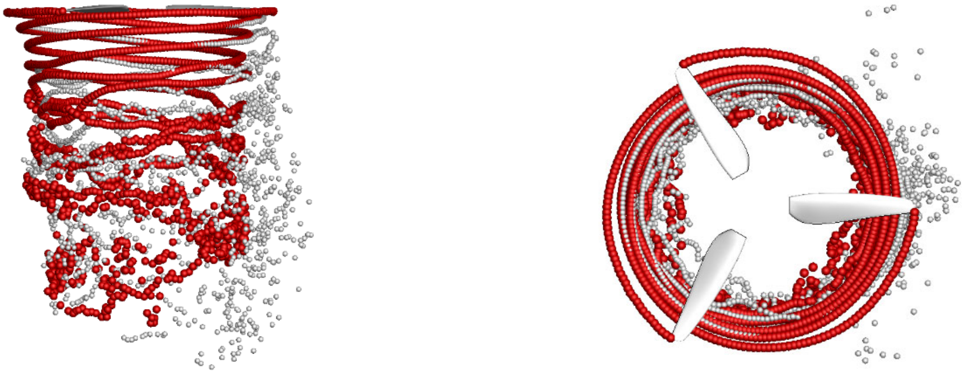

Figure 8: Loss of coherence in the wake structure produced by the propeller-propeller interactions at $d/D = 1.02$, grey spheres, compared to the coherent structure of the isolated propeller wake – red spheres. RAMSYS simulations - XZ view (top) and XY view (bottom)

The time-averaged thrust coefficient of the secondary propeller at several phase angles with respect to the main propeller is illustrated in Figure 9. Both CIRA and DLR simulations predict, despite in an opposite way, a slight increase in the CT as the phase angle of the secondary propeller increases up to $\Delta\varphi = 60°$, followed by a decrease at $\Delta\varphi = 90°$ where the calculated CT is lower than the case of the propellers in phase. IAG, PoliMi and RM3 results are almost insensitive to the phase angle.

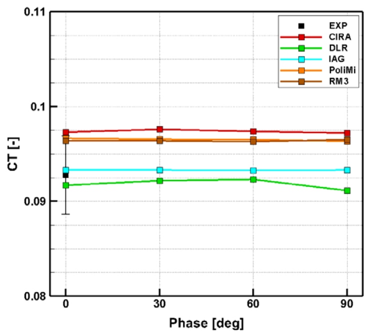

Figure 9: Thrust coefficient of the secondary propeller at several phase angles of the secondary propeller

Figure 10 shows the time-averaged thrust coefficient of the secondary propeller at the two senses of rotation of the secondary propeller, being the first one co-rotating with the main propeller, and the second one contra-rotating. PoliMi results of the contra-rotating propellers are significantly lower than those of the co-rotating propellers. Instead, all the other simulations predict almost no effect of the sense of rotation on the aerodynamic performance of the twin propellers.

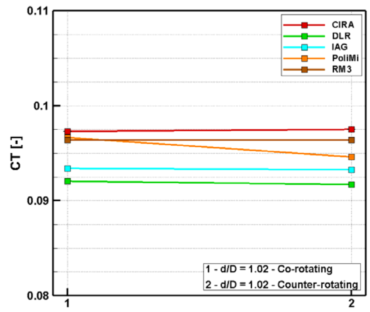

Figure 10: Thrust coefficient of the secondary propeller at the two senses of rotation of the secondary propeller

The analysis of the time-averaged torque diagram in Figure 11 shows an extremely low sensitivity of the numerical torque to the distance between the propellers' axes, with the only exception of RM3. As expected, the inviscid simulations produced significantly lower values of the torque. The higher fidelity solvers produced results closer to the experimental value but none of them was able to evaluate the reduction in torque passing from the single propeller to the twin propellers.

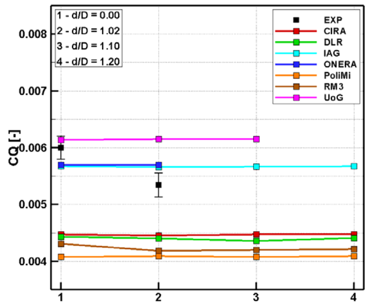

Figure 11: Torque coefficient of the secondary propeller at several distances between the twin propellers

Figure 12 and Figure 13 show the time-averaged torque diagrams at several phase angles of the secondary propeller and at the two senses of rotation of the secondary propeller, respectively. In both cases the predictions are almost insensitive to the different configurations.

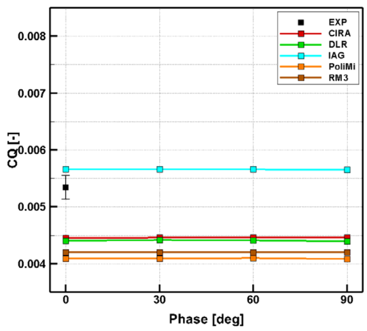

Figure 12: Torque coefficient of the secondary propeller at several phase angles of the secondary propeller

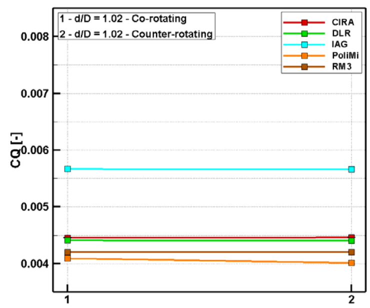

Figure 13: Torque coefficient of the secondary propeller at the two senses of rotation of the secondary propeller

Time-histories of the thrust coefficient

The thrust coefficient time history of the single propeller, Hov01, is illustrated in Figure 14.

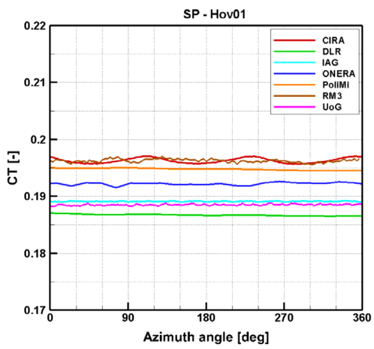

Figure 14: Thrust coefficient time histories for the single propeller - Hov01

It exhibits an almost steady behaviour. The fluctuations in CIRA results are likely produced by the interaction of the blade wakes with the support structure (pylon).

The twin propellers time histories show marked $6/rev$ fluctuations in all simulations at $d/D = 1.02$, Hov02, which are the result of strong interactional effects between the two propellers. The (relative) large azimuth step used by ONERA might result in an artificial underestimation of those fluctuations. As the distance between the two propellers increases, these effects are progressively weaker. CIRA results exhibit a minor reduction in amplitude and prevailing $3/rev$ oscillations. IAG results still show a 6/rev behaviour but the amplitude is almost zeroed. PoliMi and UoG results show an extremely low unsteadiness. Unlike the other simulations, DLR results show an increase in amplitude at $d/D = 1.10$, Hov12.

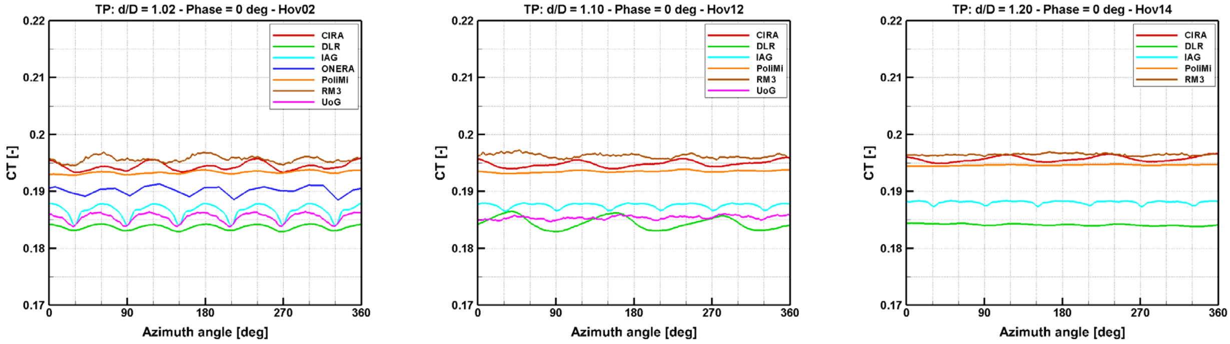

Figure 15: Thrust coefficient time histories for the twin propellers in phase at several distances of the axes of rotation: $d/D = 1.02$ - Hov02; $d/D = 1.10$ - Hov12 and $d/D = 1.20$ - Hov14

Figure 16 illustrates the thrust coefficient time histories for the twin propellers at $d/D = 1.02$, and several phase angles of the secondary propeller. Unlike the case with the twin propellers in phase, where $6/rev$ fluctuations are clearly observable, all simulations highlight that the three phase angles investigated produce $3/rev$ fluctuations with higher amplitudes, particularly at $\Delta\varphi = 60°$.

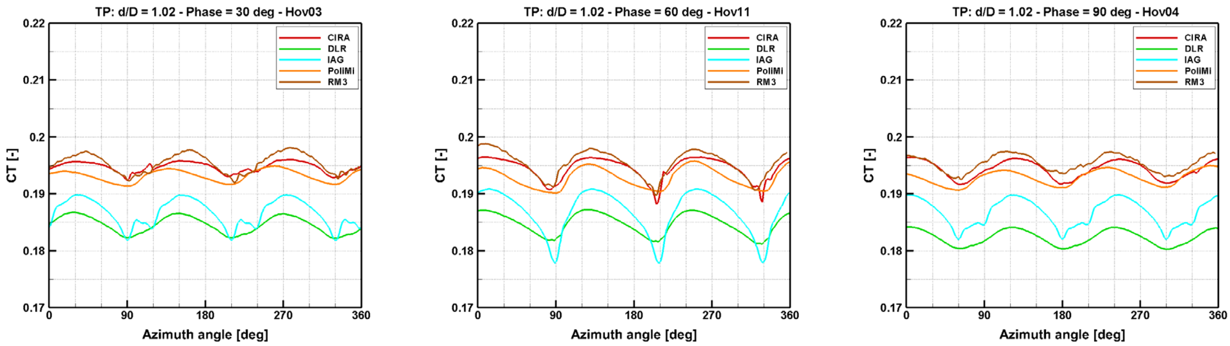

Figure 16: Thrust coefficient time histories for the twin propellers at $d/D = 1.02$, at several phase angles of the secondary propeller: $\Delta\varphi = 30°$ - Hov03; $\Delta\varphi = 60°$ - Hov11 - and $\Delta\varphi = 90°$ - Hov04

Finally, Figure 17 shows the thrust coefficient time histories for the contra-rotating twin propellers at $d/D = 1.02$ - Hov16. As for the case with phase angle $\Delta\varphi = 60°$, high amplitude, $3/rev$ fluctuations can be observed. This is because, for these two test conditions only, there is a $3/rev$ perfect alignment of the two propellers' blades along the horizontal inter-axis line ($\psi = 270°$ for the main propeller and $\psi = 90°$ for the secondary propeller, according to Figure 3), which produces the maximum interactional effect. IAG results show much stronger fluctuations.

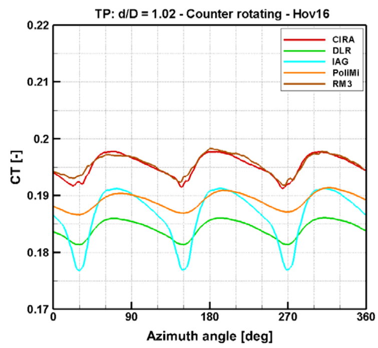

Figure 17: Thrust coefficient time histories for the contra-rotating propellers twin propellers at $d/D = 1.02$ - Hov16

PIV measurements

PIV measurements were carried out by CIRA to evaluate the details of the propellers' downwash in terms of the vertical component w of the velocity induced by the wake system. These measurements enabled a more exhaustive validation of the numerical solvers but also represented the opportunity for CIRA to extend the PIV field of investigation downstream of the propeller disks, which in literature are usually limited to no more than one rotor radius. A detailed description of the investigation procedure, combined with a Γ_2 vortex detection criterion, can be found in Ref. 56. The PIV measurements were elaborated both in instantaneous and time-averaged maps. The latter one was used to extract the vertical component w of the velocity induced at several distances below the propellers' disks as shown in Figure 18.

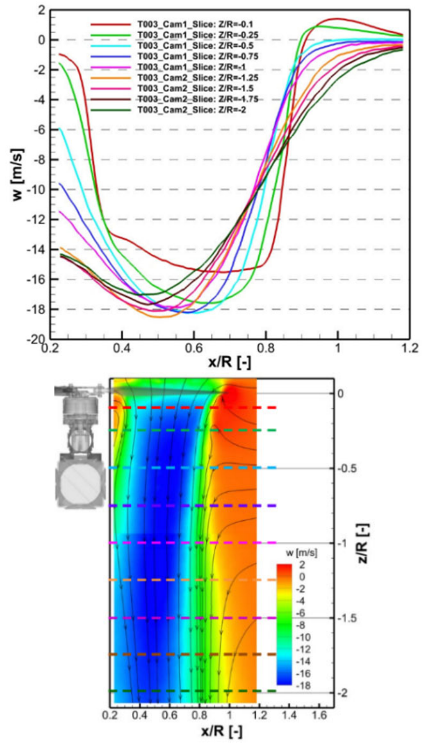

Figure 18: Time-averaged PIV measurements - Radial distributions of the vertical component of the induced velocity (top) at several heights below the propeller disks (bottom)

Numerical vs experimental comparisons of the radial distribution of the w component of the induced velocities are presented for all test cases.

For the single propeller test case, Hov01, Figure 19, four main regions can be identified in the induced velocity maps: the propeller hub region; the maximum acceleration below the disk; the shear layer boundary and slope; and the blade tip region.

In the proximity of the propeller disk ($z/R = -0.10$ and -0.25) the slope of the experimental results at the hub is predicted in a different way by some methodologies, mainly because the hub was not modelled by all partners and also because different blade root cut-outs were applied. Further downstream, the experimental slope is correctly predicted by all the simulations.

The maximum acceleration down the propeller disk is estimated in a similar manner by all solvers up to the station at $z/R = -0.50$. More downstream, all simulations, with the exception of PoliMi at $z/R = -2.00$, predict a higher velocity compared to the experimental data, and CIRA results are particularly overestimating in the lowest regions ($z/R = -1.50$ and -2.00). This occurrence gives an indication of the different dissipative nature of the solvers applied.

Regarding the shear layer region, the differences with the experimental results are explained by the diffusion produced by the viscous effects, which causes a marked thickening and reduced slope of the experimental shear layer moving downstream from the rotor disk, and which is instead modelled in some solvers by using vortex core models. Their selection and fine tuning are a key point for a correct modelling of the wake shape and the viscous effects on the velocity field. Excepting PoliMi results, which are in a better agreement with the experiment, all the other solvers, regardless of the methodology, show a similar behaviour up to $z/R = -1.50$, with the position slightly more inboard than the experimental data at the lower positions below the propeller disk. $At\, z/R = -2.00$ the predictions are extremely various.

The region around the blade tip (r/R = 1) shows that the URANS simulations by UoG are generally in good agreement with the experiment. The other simulations show a tendency to overestimate the upwash in the region between $z/R = -0.10$ and -1.00, whereas different behaviours among the solvers are shown in the lower regions.

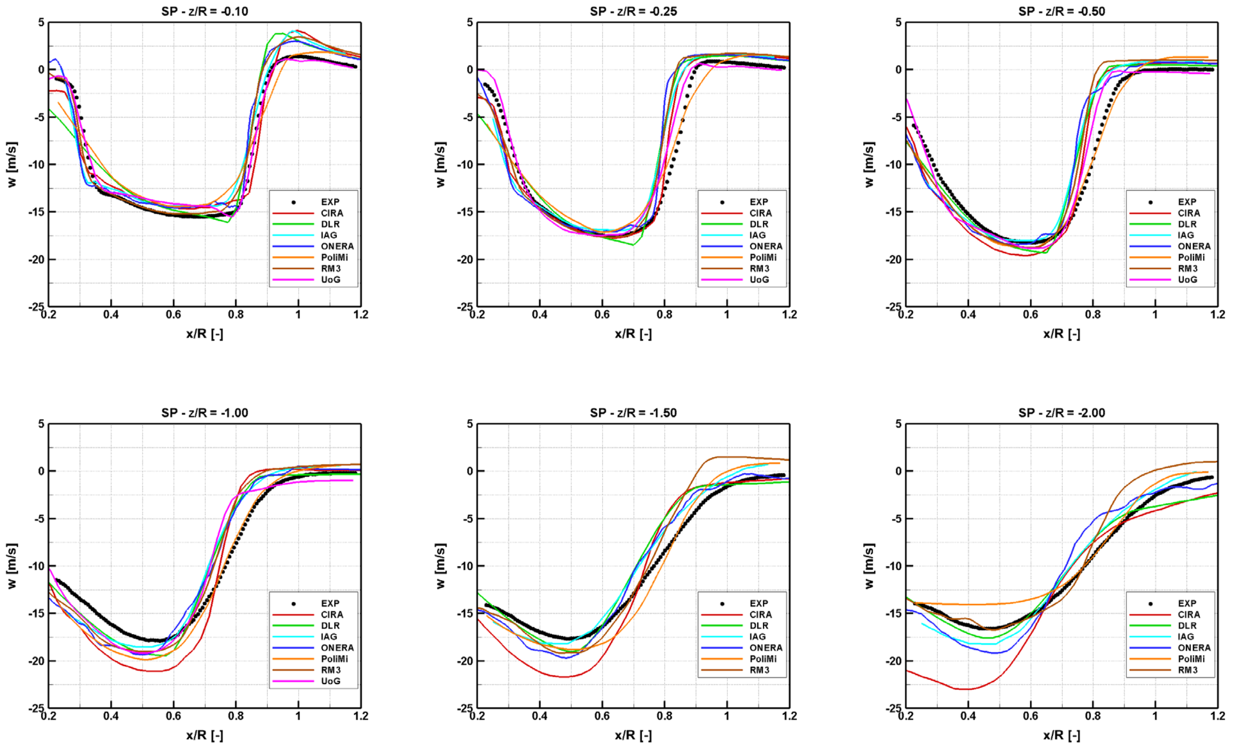

Figure 19: 2C-PIV: Numerical experimental comparisons – Single Propeller – Hov01

The PIV measurements of the twin propellers were mainly focussed on the region between the two axes of revolution, whereas the simulations were extended more outboard on both sides.

The analysis of the results shows similar numerical and experimental trends and behaviours for all the test cases investigated, Figure 20 to Figure 26.

The best agreement is always observed in the zone closer to the propellers' disks up to $z/R = -0.50$. In this zone, between the tips of the two propellers, all simulations, with the exception of PoliMi in some cases, produced an upwash or a lower downwash. Furthermore, the experimental results show a shift in the peak of the induced velocity that is not captured by any numerical result. Instead, the maximum value of the downwash is correctly evaluated by all the simulations.

Further downstream, in the zone between $z/R = -1.00$ and $z/R = -2.00$, the numerical-experimental comparison becomes more critical. With the exception of the RANS results by IAG, which show a general better agreement with the experiment in all test cases, the other simulations exhibit discrepancies of different natures. In particular, and especially at $z/R = -1.50$ and $z/R = -2.00$, CIRA predicts an excessive downwash, whereas the results of the other simulations have different behaviours depending on the test case.

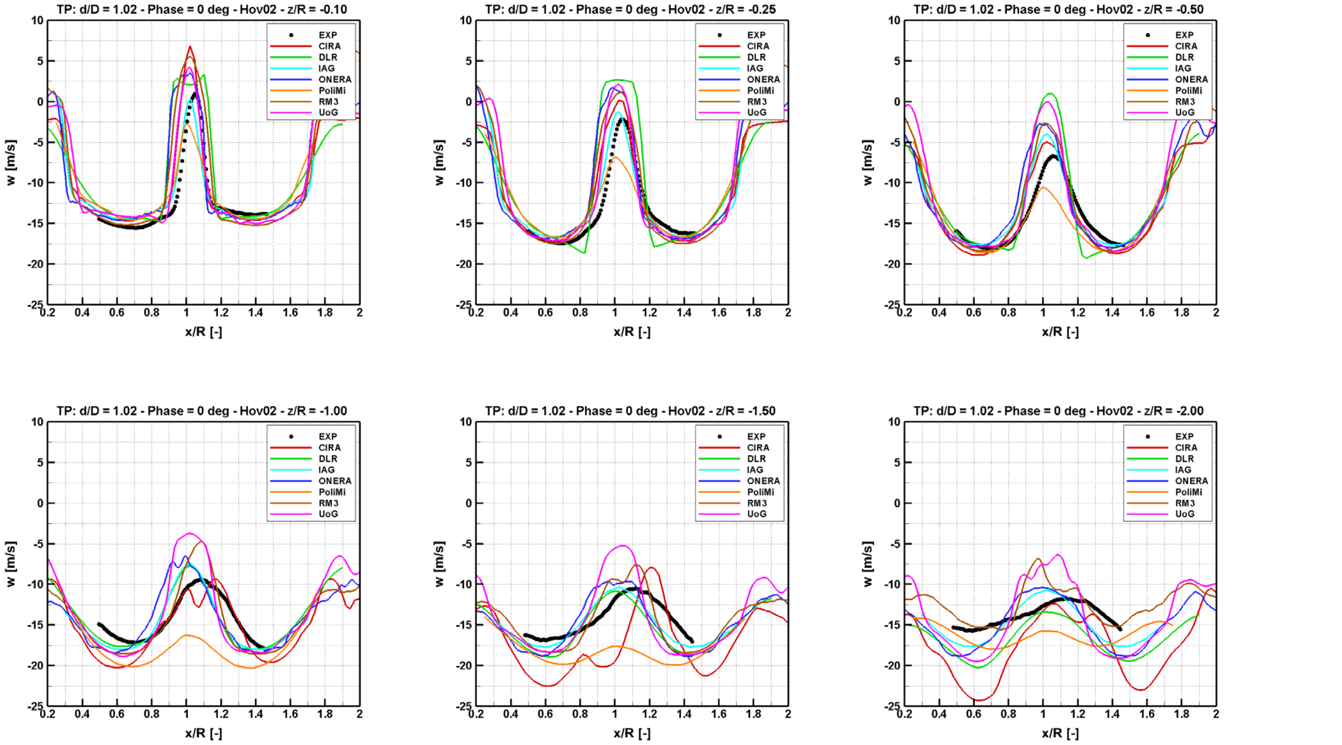

Figure 20: 2C-PIV: Numerical experimental comparisons – Twin propellers in phase, $d/D = 1.02$ – Hov02

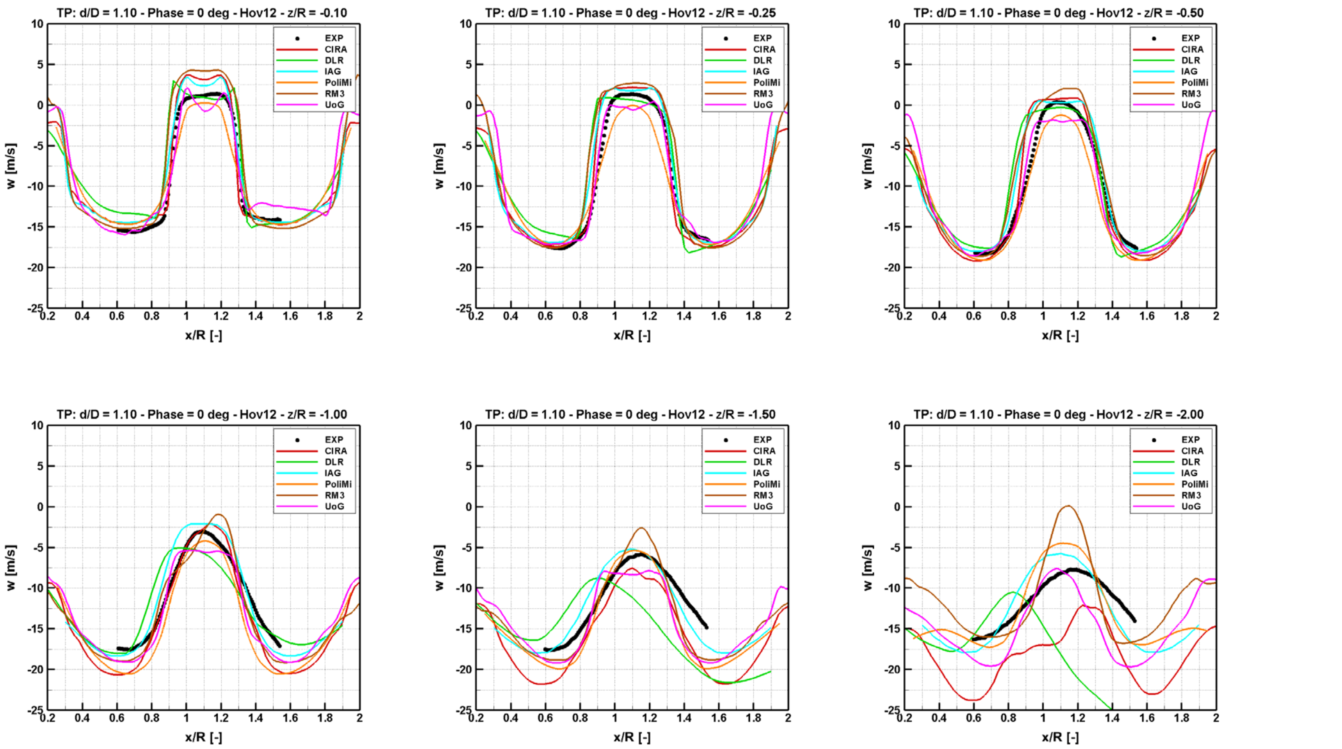

Figure 21: 2C-PIV: Numerical experimental comparisons – Twin propellers in phase, $d/D = 1.10$ – Hov12

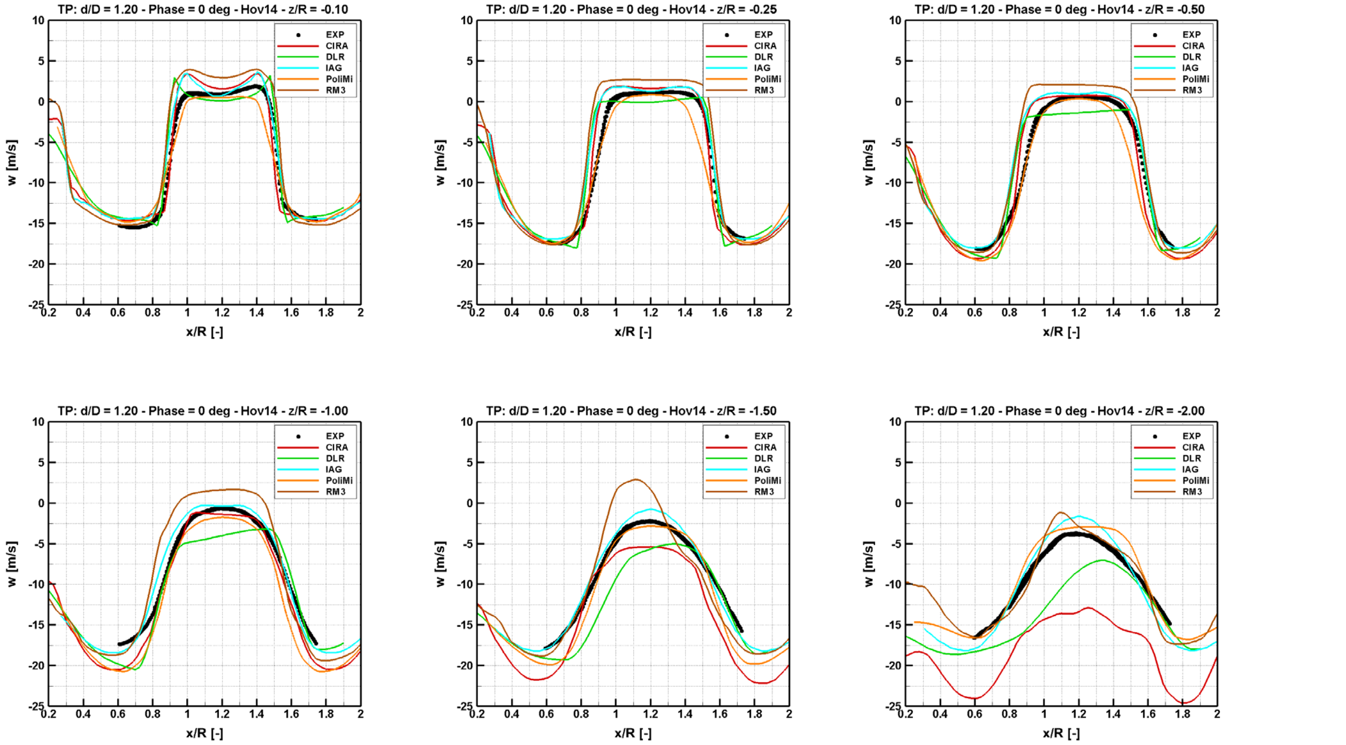

Figure 22: 2C-PIV: Numerical experimental comparisons – Twin propellers in phase, $d/D = 1.20$ – Hov14

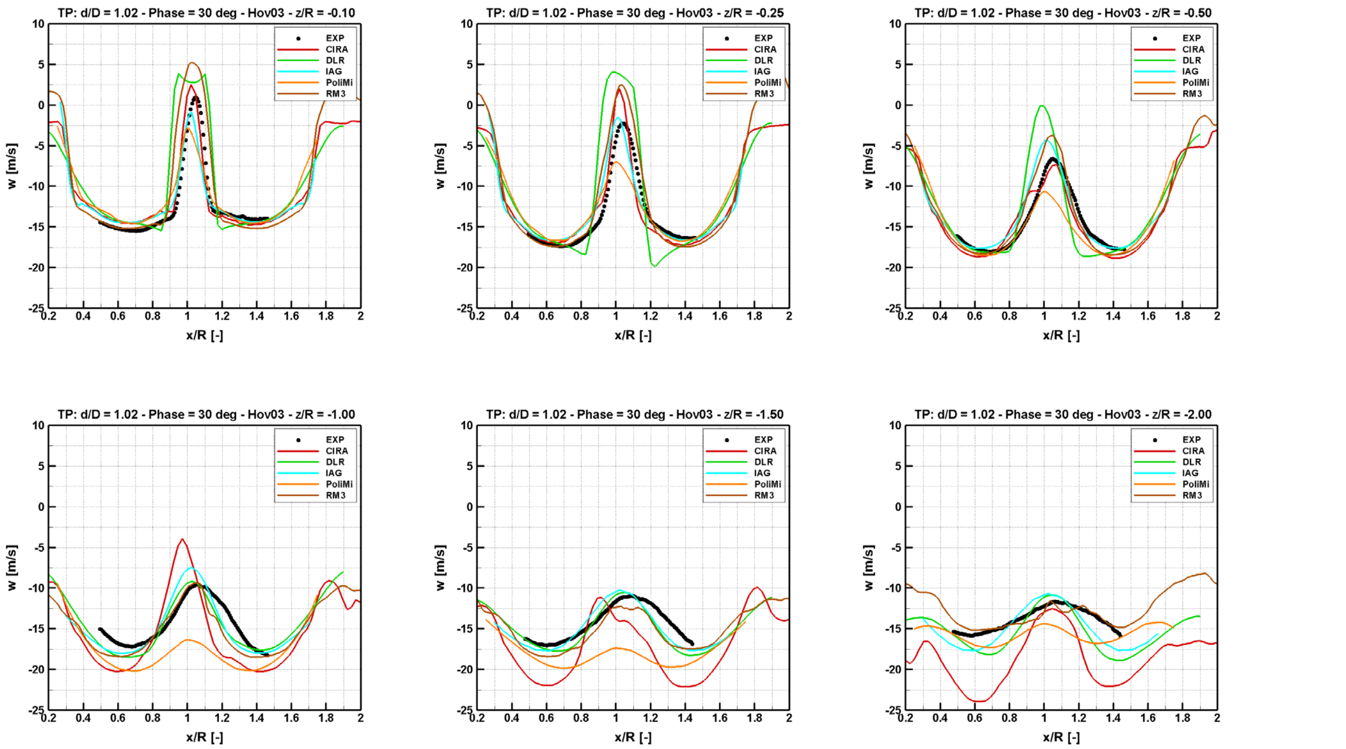

Figure 23: 2C-PIV: Numerical experimental comparisons – Twin propellers, $\Delta\varphi = 30°$, d/D = 1.02 – Hov03

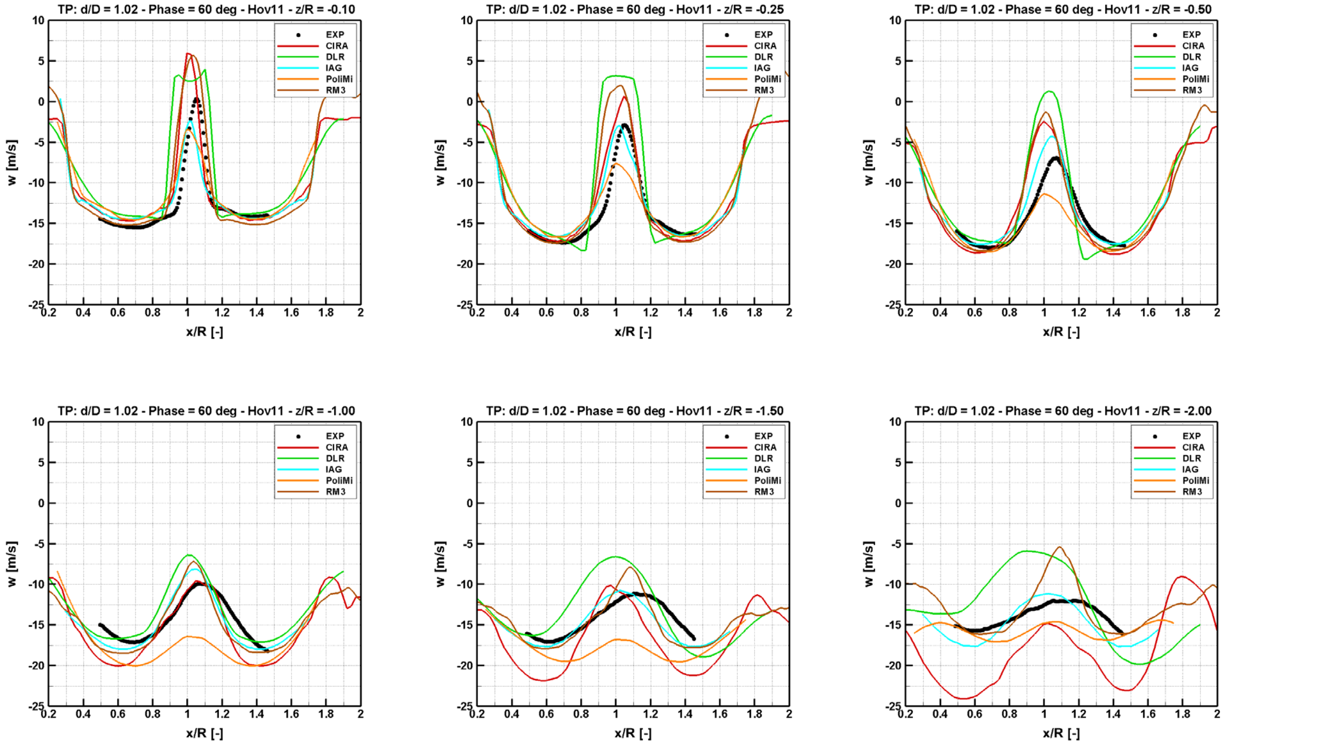

Figure 24: 2C-PIV: Numerical experimental comparisons –Twin propellers, $\Delta\varphi = 60°$, d/D = 1.02 – Hov11

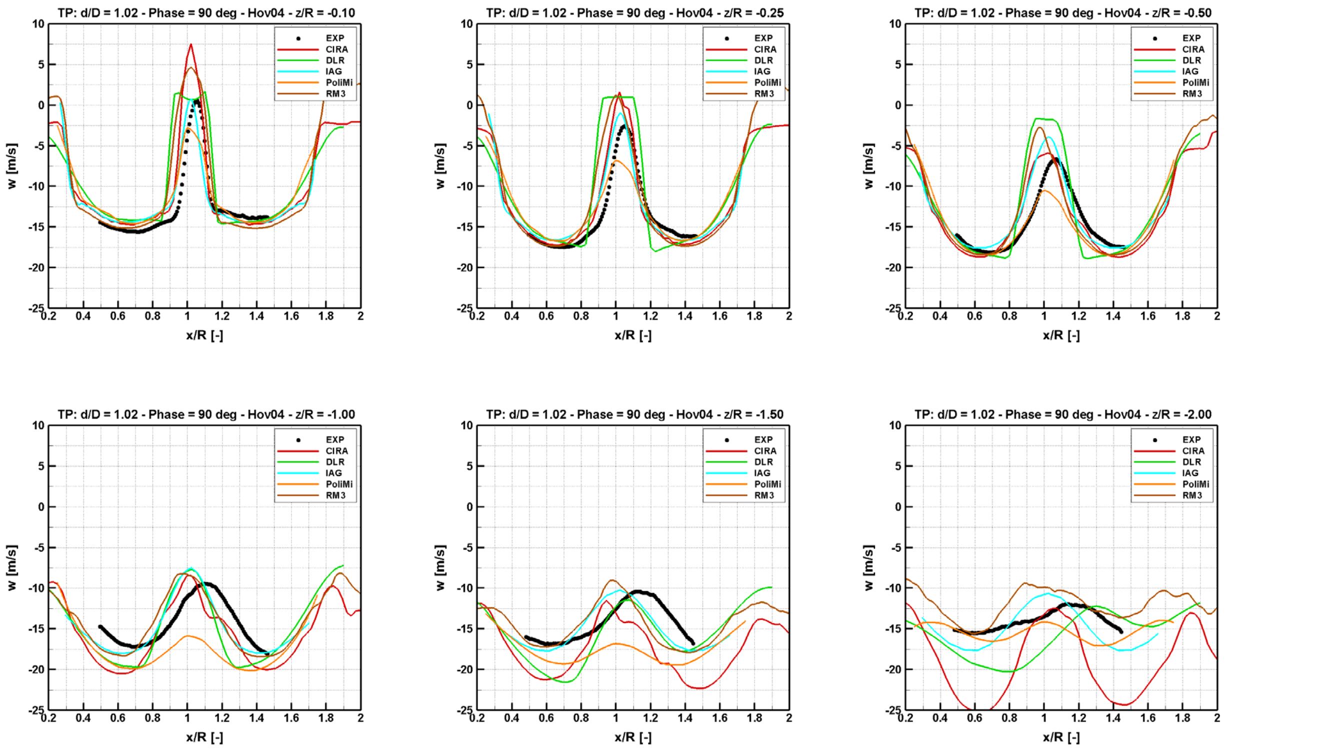

Figure 25: 2C-PIV: Numerical experimental comparisons – Twin propellers, $\Delta\varphi = 90°$, d/D = 1.02 – Hov04

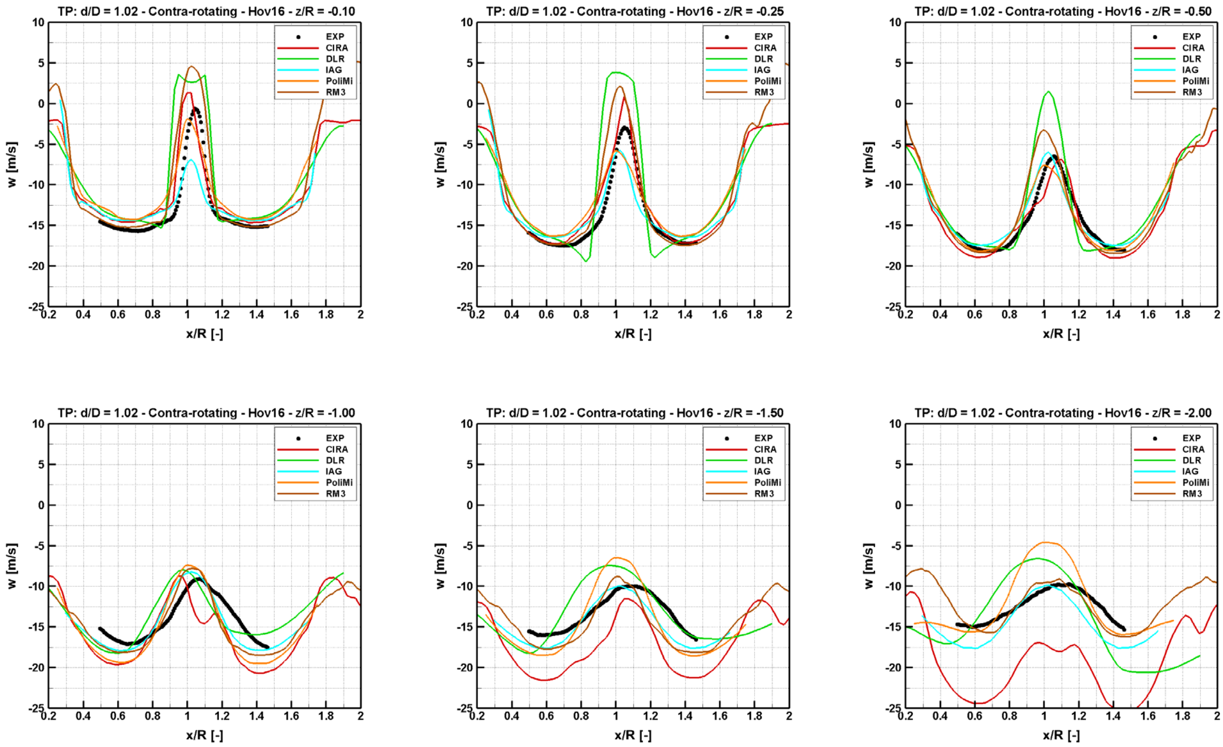

Figure 26: 2C-PIV: Numerical experimental comparisons – Twin Propellers contra-rotating, $d/D = 1 - 02$ – Hov16

6.2. Acoustic performance

The analysis of the acoustic performance was carried out by investigating the first four BPFs of each test case.

<u>Twin propellers in phase. Effect of increasing the inter-axis distance</u>

These results are shown in Figure 27, Figure 28 and Figure 29. In general, good comparisons are observed for BPF1, which is more related to the steady loading noise. At higher harmonics, the deviations in the comparison increases, thus indicating the difference in the unsteady aerodynamics predicted by the different solvers. For BPF1, almost all results indicate a minimum noise along the rotor axis (90° and 270°), except IAG. At 270°, the higher value shown in the experimental results is caused by the microphone self-noise due to the effect of the propeller downwash on microphone.

The analysis of the first BPF (BPF1) shows that the increase in the distance between the two axes of rotation does not produce any significant change in the experimental results and in the numerical data produced by IAG. With the exception of CIRA, the other numerical simulations predict two marked lobes, with respect to the plane orthogonal to the propellers' plane, at the distances $d/D = 1.02$ and 1.20. The fact that CIRA results do not show the same behaviour is explained by the pylon's effect, not accounted for in the other partners' simulations, producing more aerodynamic unsteadiness mainly radiating in direction of the rotor axis.

At the second BPF (BPF2), the experimental data show a reduction in the propellers' plane when compared to BPF1. There are no significant changes in the plane orthogonal to the propeller disks nor by increasing the distance d/D. The numerical results show a reduction in SPL compared to BPF1, which becomes progressively more significant as the distance d/D increases as the higher harmonics are more affected by the unsteady loading.

The results of the third BPF (BPF3), compared to those of BPF2, show a further reduction in the propellers' plane only for the experimental results, whereas an omnidirectional reduction, which further reduces by increasing the distance d/D, is observed in the numerical results.

The experimental data of the fourth BPF (BPF4) show an observable reduction with respect to BPF3 in the propellers' plane and only a slight reduction in the plane orthogonal to the propellers. The numerical results are quantitatively similar to those of BPF3.

Finally, it is worth mentioning the fact that, except at BPF1, all simulations tend to underestimate the experimental results, excluding UoG ones which, in some cases, show a qualitative and quantitative better agreement.

Effect of changing the phase of the secondary propeller (Twin propellers at d/D = 1.02).

These results are shown in Figure 30, Figure 31 and Figure 32.

The numerical and experimental SPLs at BPF1 show an increase in the plane orthogonal to the propellers with respect to the case with the two propellers in phase, Figure 27. The experimental results show a general dissymmetry in the propellers' plane with a higher reduction at the azimuth angle $\psi = 0°$. The numerical results show an opposite dissymmetry for the phase angles $\Delta\varphi = 30°$ and $\Delta\varphi = 90°$, and no dissymmetry at $\Delta\varphi = 60°$. This behaviour is explained by the fact that only at $\Delta\varphi = 60°$ there is a perfect symmetry of the two propellers, every 120°, with respect to the mid-plane between the two propeller hubs. Furthermore, partners' simulations predict the dissymmetry in the opposite way. In particular, CIRA and PoliMi predict the same behaviour which is opposite to that of the other partners.

At BPF2,the experimental results show an increase in SPL, with respect to the propellers in phase, Figure 27, in the propellers' plane with a slight increase in the dissymmetry, as for BPF1, but only at the phase angle $\Delta\varphi = 90°$, Figure 32. The cases in phase, Figure 27, and at the phase angle $\Delta\varphi = 60°$, Figure 31, produce SPL values in the plane orthogonal to the propellers that are similar but slightly greater than the cases with the phase angles $\Delta\varphi = 30°$ and $\Delta\varphi = 90°$, Figure 30 and Figure 32, respectively. The numerical results show two marked lobes with respect to the propellers' plane and a higher noise in the propellers' plane with respect to the case in phase. The propellers with the phase angle $\Delta\varphi = 60°$ show a marked increase in noise in the plane orthogonal to the propellers too.

The experimental results of BPF3 do not show significant changes with respect to BPF2. The numerical predictions show an increase in the SPL in the plane orthogonal to the propellers with respect to the propellers in phase, Figure 27. This increase is even more evident for the propeller with phase angle $\Delta\varphi = 60°$, Figure 31. Significant quantitative differences can be observed between IAG results and all the other ones.

The same general considerations made for BPF3 hold for BPF4 too. Furthermore, there are no relevant noise reductions at BPF4 with respect to BPF3.

Effect of sense of rotation of the secondary propeller (Twin propellers in phase at d/D = 1.02).

The results for the contra-rotating propellers are shown in Figure 33 and are compared with those of the co-rotating propellers, Figure 27.

Regarding BPF1, both numerical and experimental results of the contra-rotating, propellers show an omnidirectional increase in noise with respect to the case of the co-rotating propellers.

At BPF2, both numerical and experimental results show a more uniform distribution of SPL around the contra-rotating propellers with respect to the co-rotating ones. No significant quantitative changes can be observed.

The numerical results for BPF3 show an increase in the noise, with respect to the case of co-rotating propellers, which is more evident in the plane orthogonal to the propellers. In this case too, the azimuthal noise distribution is more uniform.

At BPF4 there are no significant quantitative between the co-rotating and contra-rotating propellers. The azimuthal noise distribution is more uniform.

In general, some qualitative similarities with the case at phase angle $\Delta\varphi = 60°$, Figure 31, can be observed.

Single propeller

With the exception of BPF1, where the numerical prediction and the experimental results differ only in the plane orthogonal to the propellers, the other BPFs show significant differences between the experiment and the simulations. In particular, by increasing the BPF, the experimental results show slight changes, more markedly only at BPF4. Conversely, the numerical results show a significant and progressive reduction by increasing the BPF, Figure 34. A possible explanation can be found in the presence of the pylons (also hypothesised by Zarri et al. in Ref. 8) only modelled in CIRA simulations but not in the other ones. In general, the noise produced by the isolated propeller at higher BPFs is always lower than that produced by the twin propellers, regardless of the operative condition.

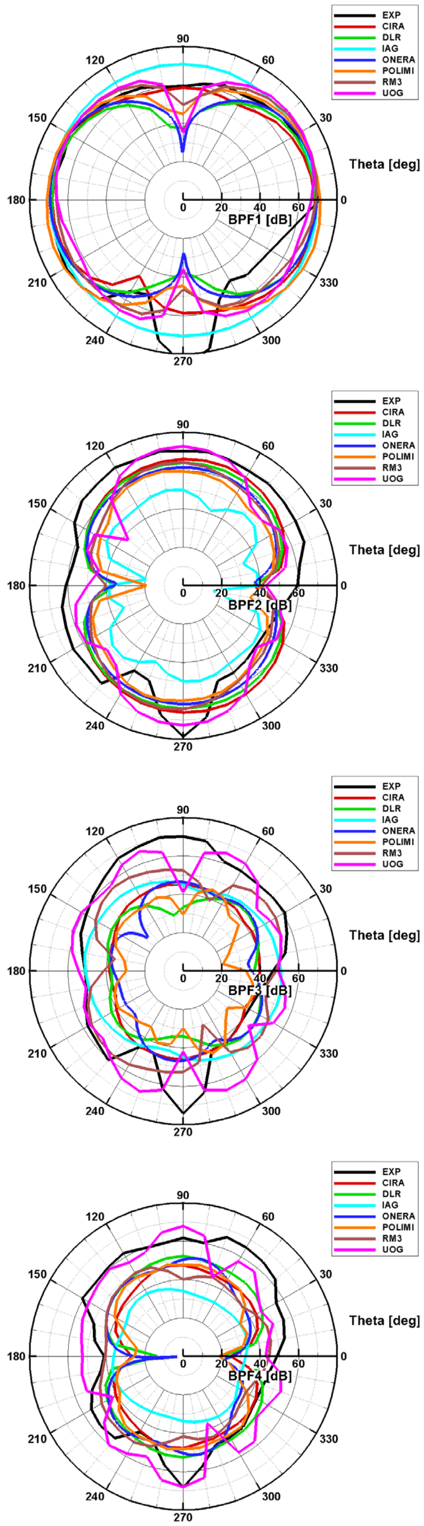

Figure 27: BPF SPL (dB) - Twin propellers - d/D = 1.02 – Hov02

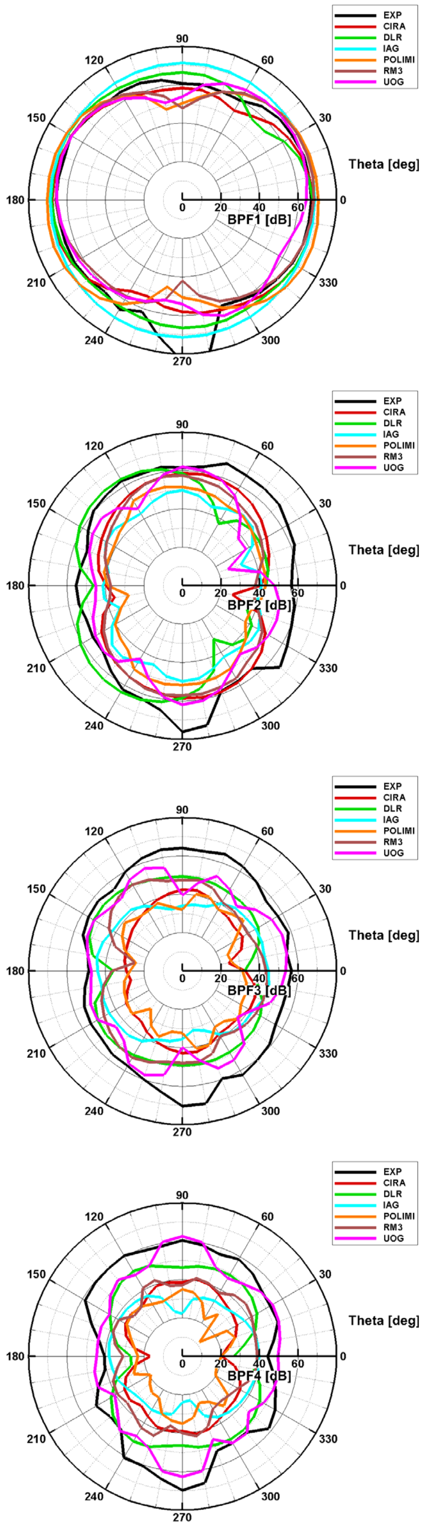

Figure 28: BPF SPL (dB) - Twin propellers - d/D = 1.10 – Hov12

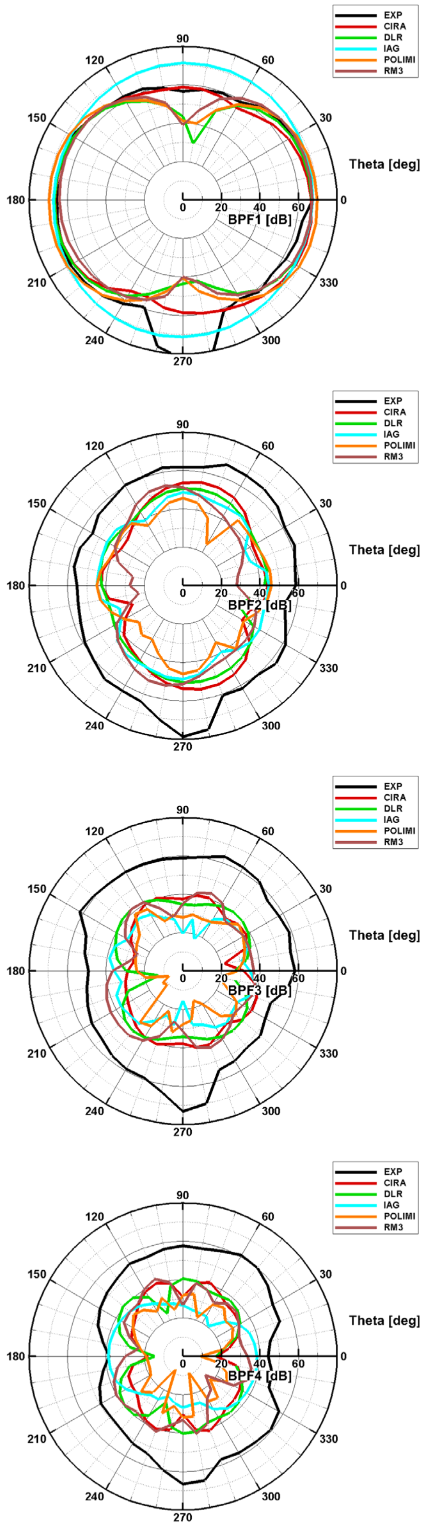

Figure 29: BPF SPL (dB) - Twin propellers – d/D = 1.20 – Hov14

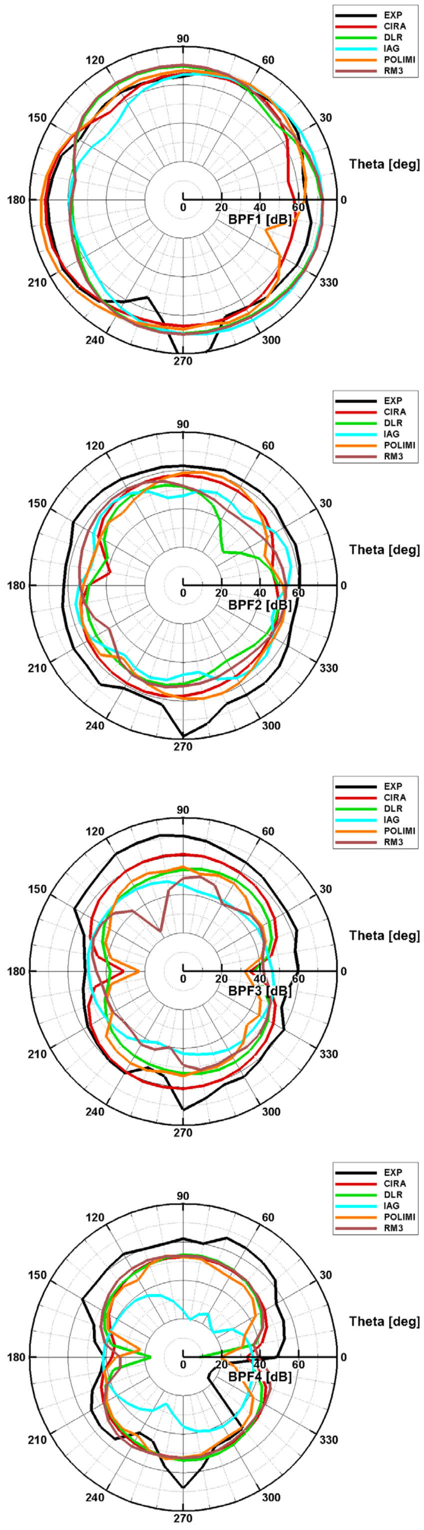

Figure 30: BPF SPL (dB) - Twin propellers - d/D = 1.02 - Phase +30° – Hov03

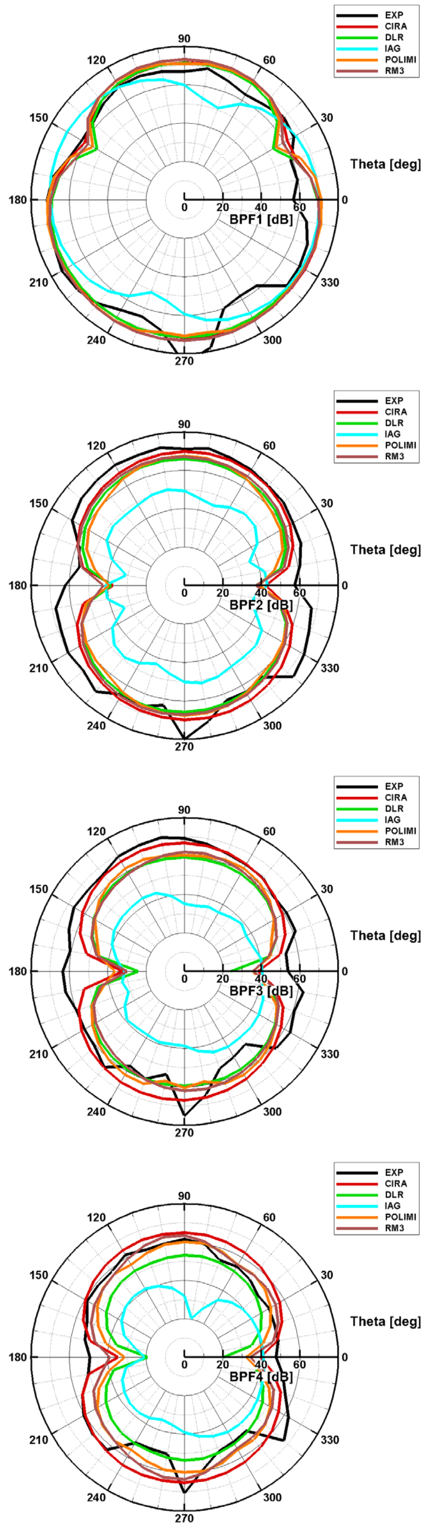

Figure 31: BPF SPL (dB) - Twin propellers - d/D = 1.02 – Phase +60° - Hov11

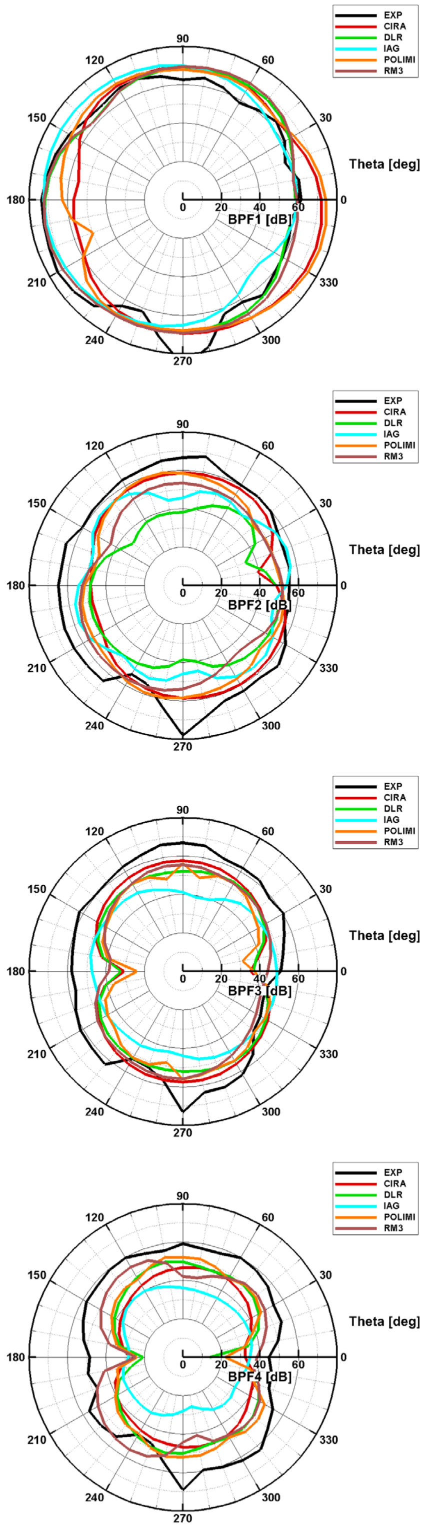

Figure 32: BPF SPL (dB) - Twin propellers - d/D = 1.02 - Phase +90° – Hov04

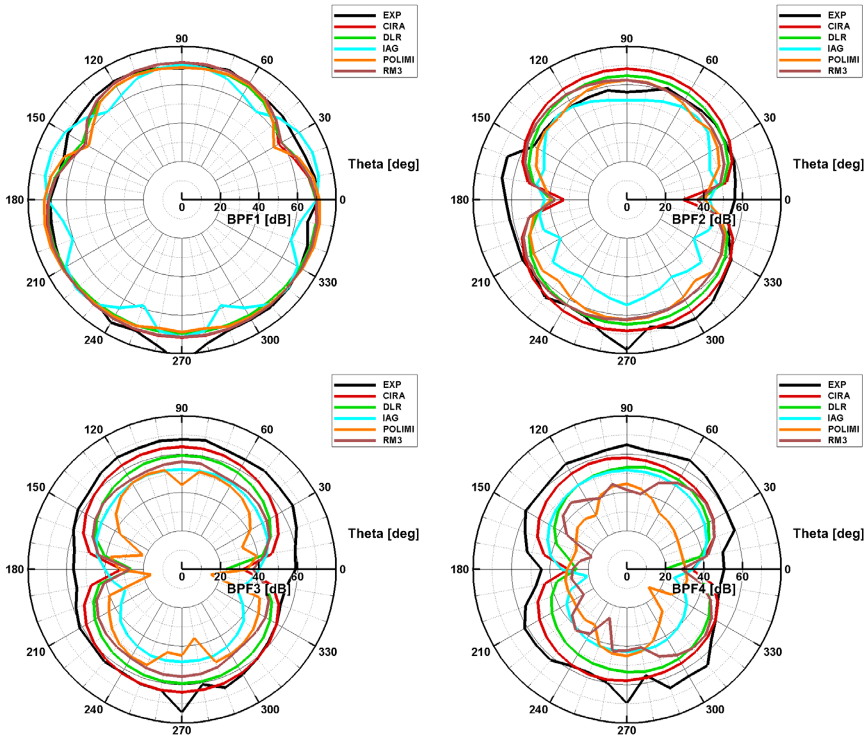

Figure 33: BPF SPL (dB) - Twin propellers – d/D = 1.02 Contra-rotating – Hov16

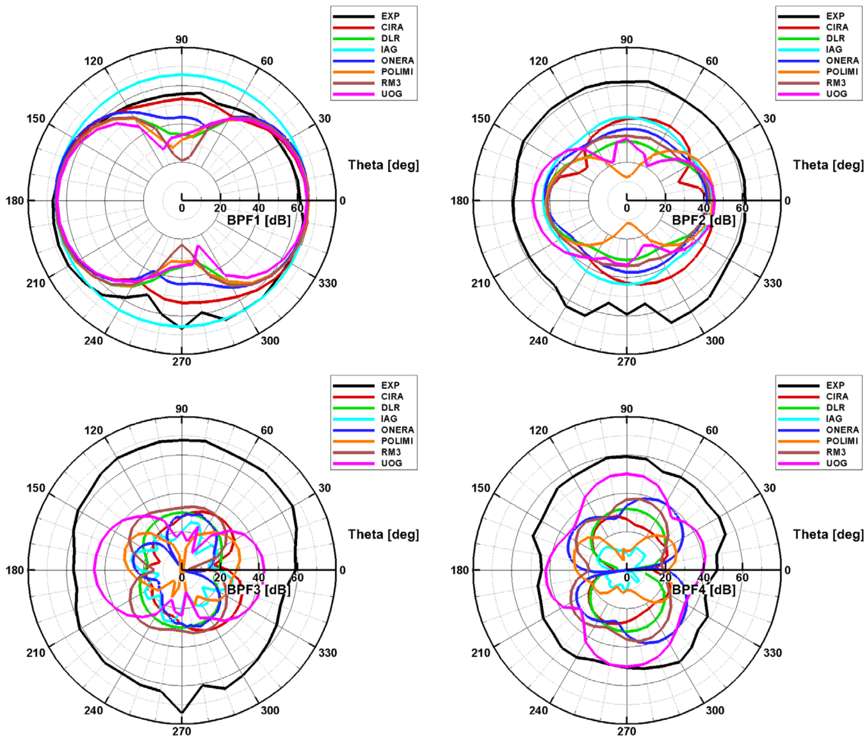

Figure 34: BPF SPL (dB) - Single propeller - Hov01

7. CONCLUSIONS

The paper illustrated numerical-experimental investigations carried out by the consortium of the GARTEUR Action Group AG-26 “Noise Radiation and Propagation for Multirotor System Configurations” concerning the aerodynamics and acoustics of single and twin co-rotating propeller configurations in hover flight. The activity was aimed at evaluating the effect of: 1) the inter-axis distance between the twin-propellers; 2) the phase angle of the secondary propeller with respect to the main one; 3) the sense of rotation of the secondary propeller with respect to the main one on the aeroacoustic properties of the examined configurations. Loads, PIV, and microphone measurements were jointly conducted by CIRA and Cusano University at CIRA, in a laboratory environment and in a semi-anechoic chamber.

The main results obtained are summarized in the following.

From the aerodynamic standpoint, it was generally observed that:

- the thrust coefficient of each of the two twin-propellers reduces with respect to that of the single propeller. This behaviour was explained by the sudden breakdown of the coherent vortical structures that were instead observed to develop downstream of the single propeller. This reduction is higher when the two propellers are closer to each other, and decreases asymptotically by increasing the separation distance. This effect was correctly simulated by all numerical results, regardless of the methodology applied, but with a milder and different amount of reduction;

- the experimental torque coefficient follows the same trend as the thrust. Conversely, all the simulations look almost insensitive to the effect of increasing the distance between the axes of rotation. As expected, the potential methodologies significantly underestimate the torque;

- de-phasing or changing the sense of rotation of the secondary propeller produces almost negligible effects in both thrust and torque coefficients;

- the analysis of the thrust coefficient time histories evaluated by all numerical solvers highlighted an almost steady behaviour for the single propeller, and a 6/rev behaviour for the twin propellers in phase with decreasing amplitude as the distance between the propellers increased. Instead, depashing or changing the sense of rotation of the secondary propeller produced marked 3/rev fluctuations with amplitude reaching its highest value at $\Delta\varphi$=60° and for the contra-rotating propellers. This result was explained by considering that these two conditions are the only cases where the blades of the two propellers are perfectly aligned along the line joining the two hub centres, at each 120°, thus minimizing the distance between the two blade tips;

- the w component of the velocity induced at several vertical distances below the propellers’ disks was measured and numerically predicted to provide a deeper insight into the flow field produced by the configurations examined. The analysis highlighted a reasonable agreement between all solvers and the experiment up to a distance from the rotor disks of z/R = -0.50. Further downstream, overestimations in the velocity were observed in almost all simulations, particularly in CIRA results. This behaviour can be justified by the different dissipative properties of the numerical methodologies applied. In the specific case of the twin propellers, the numerical results produced an upwash or a lower downwash in the region between the axes of revolution of the two propellers. On average, the URANS results produced by IAG produced a closer agreement with the experiment.

Regarding the acoustic results, it was observed that:

- the agreement between the experimental and all numerical results is globally reasonable at the BPF1, while some discrepancies can be detected at the BPF2. Regarding the last two BPFs investigated, all numerical results underestimate, with a different degree, the experiment. In particular, significant differences can be observed for the BPF2, 3 and 4 of the single propeller. The reason is likely due to the presence of the pylons, not modelled in all simulations.

- the increasing distance between the two propellers reduces the noise because the interactional effects decrease progressively;

- de-phasing the secondary propeller is, in general, not beneficial for the noise as it produces an increase in the amplitude of the load fluctuations;

- in the particular cases of the phase angle $\Delta\varphi = 60°$ and contra-rotating propellers, the close proximity of the blade tips along the line joining the two hub centres produces the maximum increase in the amplitude of the load fluctuations, which maximizes the noise.

Author contact:

Antonio Visingardi a.visingardi@cira.it

Mattia Barbarino m.barbarino@cira.it

Fabrizio De Gregorio f.degregorio@cira.it

Luca Greco luca.greco@cnr.it

Claudio Testa claudio.testa@cnr.it

Stefano Zaghi stefano.zaghi@cnr.it

Paolo Candeloro paolo.candeloro@unicusano.it

Tiziano Pagliaroli tiziano.pagliaroli@unicusano.it

Giovanni Bernardini giovanni.bernardini@uniroma3.it

Caterina Poggi caterina.poggi@uniroma3.it

Luca Abergo, luca.abergo@polimi.it

Alberto Guardone alberto.guardone@polimi.it

Andrea Cavalli, andrea6.cavalli@mail.polimi.it

Daniele Granata, daniele.granata@polimi.it

Alex Zanotti alex.zanotti@polimi.it

Jianping Yin jianping.yin@dlr.de

Florian Fausel

Manuel Keßler kessler@iag.uni-stuttgart.de

Moritz Muth moritz.muth@iag.uni-stuttgart.de

Gabriel Reboul gabriel.reboul@onera.fr

George Barakos george.barakos@glasgow.ac.uk

Geng Qiao g.qiao.1@research.gla.ac.uk

8. ACKNOWLEDGMENTS

The numerical and experimental investigations described in the present paper were all carried out by the authors in the framework of the GARTEUR Action Group 26: “Noise Radiation and Propagation for Multirotor System Configurations” promoted by the Rotorcraft Group of Responsables.

9. REFERENCES

1. EASA. Study on the societal acceptance of Urban Air Mobility in Europe. May 2021;

2. Zhou, W., Ning, Z., Li, H., Hu, H., “An experimental investigation on rotor-to-rotor interactions of small UAV propellers,” 35th AIAA Applied Aerodynamics Conference, Denver, CO, USA, 5–9 June 2017; p. 3744. https: //doi.org/10.2514/6.2017-3744;

3. Shukla, D.; Komerath, N., “Multirotor Drone Aerodynamic Interaction Investigation,” *Drones*. 2018, 2, 43. https://doi.org/10.3390/ drones2040043.

4. Ko, J.; Kim, J.; Lee, S., “Computational study of wake interaction and aeroacoustic characteristics in multirotor configurations,” INTER-NOISE and NOISE-CON Congress and Conference Proceedings, Institute of Noise Control Engineering: Reston, VA, USA, 2019; Volume 259, pp. 5145–5156;

5. Bu, H., Wu, H., Bertin, C., Fang, Y., Zhong, S., “Aerodynamic and acoustic measurements of dual small-scale propellers,” *Journal of Sound and Vibration*. https://doi.org/10.1016/j.jsv.2021.116330, 2021;

6. Stokkermans, T., Usai, D., Sinnige, T., Veldhuis, L., “Aerodynamic interaction effects between propellers in typical eVTOL vehicle configurations,” *Journal of Aircraft*. 2021, 58, 815–833. https://doi.org/10.2514/1.C035814;

7. Zanotti, A.; Algarotti, D., “Aerodynamic interaction between tandem overlapping propellers in eVTOL airplane mode flight condition,” *Aerospace Science and Technology.* 2022, 124, 107518. https://doi.org/10.1016/j.ast.2022.107518;

8. Zarri, A., Dell’Erba, E., Munters, W., Schram, C. Aerodynamic installation effects on the sound emissions of a drone in hover. DICUAM *2022*. March 22-24, 2022;

9. https://garteur.org/;

10. Boisard, R., et al., “Rotor - Rotor Wakes Interactions” – Terms of Reference for the GARTEUR Action Group RC/AG-25, Feb. 2019;

11. Yin, J., et al., “Noise Radiation and Propagation for Multirotor System Configurations” - Terms of Reference for the GARTEUR Action Group RC/AG-26, Dec. 2021;

12. Kostek, A., Braukmann, J.N., Lößle, F., Miesner, S., Visingardi, A., Boisard, R., Riziotis, V.,

Keßler, M., Gardner, A.D, “Experimental Investigation of Quadrotor Aerodynamics with Computational Cross-Validation,” Vertical Flight Society’s 79th Annual Forum & Technology Display, West Palm Beach, FL, USA, May 16–18, 2023;

13. Kostek, A., Braukmann, J.N., Lößle, F., Miesner, S., Visingardi, A., Boisard, R., Riziotis, V., Keßler, M., Gardner, A.D., “Experimental and Computational Investigation of Aerodynamic Interactions in Quadrotor Configurations,” *Journal of the American Helicopter Society*. Vol.69, 022009 (2024), DOI:10.4050/JAHS.69.022009;

14. Nargi, R.E., Candeloro, P., De Gregorio, F., Ceglia, G., Pagliaroli, T., “Fluid-Dynamic and Aeroacoustic Characterization of Side-by-Side Rotor Interaction,” *Aerospace*, vol.10, pg. 851, 2023, https://doi.org/10.3390/aerospace10100851;

15. Yin, J., De Gregorio, Rossignol, K.S., Rottmann, L., Ceglia, G., Reboul, G., Barakos, G., Qiao, G., Muth, M., Kessler, M., Visingardi, A., Barbarino, M., Petrosino, F., Zanotti, A., Oberti, N., Galimberti, L., Bernardini, G., Poggi, C., Abergo, L., Caccia, F., Guardone, A., Testa, C., Zaghi, S., “Acoustic and Aerodynamic Evaluation of DLR Small-scale Rotor Configurations Within GARTEUR AG-26,” 49th European Rotorcraft Forum (ERF), Bückeburg, Germany, September 5–7, 2023;

16. De Gregorio, F., Candeloro, P., Ceglia, G., Pagliaroli, T, “Flow field and acoustic assessment of twin rotors in hover conditions,” XXXI AIVELA Annual Meeting, Milan, IT, December 5-6, 2023;

17. Visingardi, A., D'Alascio, A., Pagano, A., Renzoni, P., “Validation of CIRA's rotorcraft aerodynamic modelling system with DNW experimental data,” 22nd European Rotorcraft Forum, Brighton, UK, 1996. doi: http://hdl.handle.net/20.500.11881/3171.

18. Morino, L., “A General Theory of Unsteady Compressible Potential Aerodynamics,” NASA CR-2464, 1974;

19. Ffowcs Williams, J.E., and Hawkings, D.L., “Sound Generation by Turbulence and Surfaces in Arbitrary Motion,” *Philosophical Transactions of the Royal Society*, Vol. A264, No. 1151, 1969, pp. 321-542;

20. Casalino, A., “An advanced time approach for acoustic analogy predictions,” *Journal of Sound and Vibration*, 261 (4) (2003) 583{612. doi: https://doi.org/10.1016/S0022-460X(02)00986-0;

21. Casalino, D., Barbarino, M., Visingardi, A., “Simulation of helicopter community noise in complex urban geometry,” *AIAA Journal* 49 (8) (2011) 1614{1624. doi:10.2514/1.J050774;

22. Barbarino, M., Petrosino, F., Visingardi, A., “A high-fidelity aeroacoustic simulation of a VTOL aircraft in an urban air mobility scenario,” *Aerospace Science and Technology* (2021). 107104. 10.1016/j.ast.2021.107104;

23. Farassat, F., “Derivation of Formulations 1 and 1A of Farassat,” 2007;

24. Yin, J., Rossignol, K.-S., Rottmann, L., Schwarz, T., “Numerical Investigations on Small-scale Rotor Configurations with Validation using Acoustic Wind Tunnel Data,” 48th European Rotorcraft Forum, 2022, 6-8 September 2022, Winterthur, Switzerland;

25. Ahmed, S.R., Vidjaja, V.T., “Unsteady Panel Method Calculation of Pressure Distribution on BO105 Model Rotor Blades,” *Journal of the American Helicopter Society*, pp. 47-56, Jan. 1998;

26. Yin, J., Ahmed, S.R., “Helicopter main rotor/tail rotor interaction,” *Journal of the American Helicopter Society*, Vol. 45 (No. 4), pp. 293-302, 2000;

27. Yin, J., van der Wall, B.G., Wilke, G.A., “Rotor Aerodynamic and Noise under Influence of Elastic Blade Motion and Different Fuselage Modeling,” 40th European Rotorcraft Forum 2014, 2-5 September 2014, Southampton, UK;

28. CS GROUP, http://www.prolb-cfd.com;

29. Jacob, J., Malaspinas, O., and Sagaut, P., “A new hybrid recursive regularised bhatnagar-gross-krook collision model for lattice boltzmann method-based large eddy simulation,” *Journal of Turbulence*, Vol. 19, pp. 1–26;

30. Astoul, T., Wissocq, G., Boussuge, J.-F., Sengissen, A., and Sagaut, P., “Lattice Boltzmann method for computational aeroacoustics on non-uniform meshes: A direct grid coupling approach,” *arXiv*, (2004.14887);

31. Leveque, E., Toschi, F., Shao, L., and Bertoglio, J.-P., "Shear-improved Smagorinsky model for large-eddy simulation of wall-bounded turbulent flows," *Journal of Fluid Mechanics*, Vol. 570, pp. 491–502;

32. Prieur, J. and Rahier, G., "Comparison of the Ffowcs Williams-Hawkings and Kirchhoff rotor noise calculations," 4th AIAA/CEAS Aeroacoustics Conference, Toulouse, 1998;

33. Rahier, G. and Prieur, J., "An efficient Kirchhoff integration method for rotor noise prediction starting indifferently from subsonically or supersonically rotating meshes," 53rd AHS Annual Forum, Virginia Beach, USA, 1997.

34. Tugnoli, M., Montagnani, D., Syal, M., Droandi, G., and Zanotti, A., "Mid-fidelity approach to aerodynamic simulations of unconventional VTOL aircraft configurations," *Aerospace Science and Technology*, Vol. 115, 2021, p. 106804. https: //doi.org/10.1016/ j.ast.2021.106804;

35. Galimberti, L., Morelli, M., Guardone, A., and Zhou, B. Y., "Propeller Noise Prediction Capabilities within SU2," AIAA SCITECH 2023 Forum, National Harbor, MD & Online, 2023, p. 1548. https://doi.org/10.2514/6.2023-1548;

36. Gennaretti, M., Bernardini, G., Serafini, J., and Romani, G, "Rotorcraft comprehensive code assessment for blade–vortex interaction conditions," *Aerospace Science and Technology*, 2018, 80, pp. 232-246;

37. Gennaretti, M., Colella, M. M., and Bernardini, G., "Prediction of tiltrotor vibratory loads with inclusion of wing-proprotor aerodynamic interaction," *Journal of Aircraft*, Vol. 47, No. 1, 2010, pp. 71–79.

38. Leone, S., Testa, C., Greco, L., Salvatore, F., "Computational analysis of self-pitching propellers performance in open water," *Ocean Engineering*. 2013. 64, 122–134;

39. Gennaretti M., Iemma U., Testa C. "Prediction of sound scattered by moving bodies with applications to propeller-driven airplanes" (2006) - 12th AIAA/CEAS Aeroacoustics Conference, 2, pp. 969 - 980, DOI: 10.2514/6.2006-2475.

40. Testa, C., Greco, L., Bosschers, J, "Marine propeller shaft loading analysis in moderate oblique-flow conditions," *Ocean Engineering*, 2022, 262;

41. Greco L., Testa C., Salvatore F. "Design oriented aerodynamic modelling of wind turbine performance" (2007) Journal of Physics: Conference Series, 75 (1), art. no. 012011, DOI: 10.1088/1742-6596/75/1/012011;

42. Gennaretti, M., and Bernardini, G., "Novel boundary integral formulation for blade-vortex interaction aerodynamics of helicopter rotors," *AIAA journal*, Vol. 45, No. 6, 2007, pp. 1169–1176;

43. Antoniadis, A., Drikakis, D., Zhong, B., Barakos, G., Steijl, R., Biava, M., Vigevano, L., Brocklehurst, A., Boelens, O., Dietz, M., et al., "Assessment of CFD methods against experimental flow measurements for helicopter flows," *Aerospace Science and Technology*, Vol. 19, No. 1, 2012, pp. 86–100;

44. Steininger, R., Barakos, G. N., and Woodgate, M. A., "Numerical Analysis of HVAB and STAR Rotor Blades Using HMB3," AIAA SCITECH 2023 Forum, 2023, p. 1189;

45. Barakos, G. and Johnson, C., "Acoustic comparison of propellers," International *Journal of Aeroacoustics*, Vol. 15, No. 6-7, 2016, pp. 575–594, DOI: 10.1177/1475472X16659214;

46. Qiao, G., "Parametric study of aerodynamic performance of equivalent ducted/un-ducted propellers based on high-fidelity computational fluid dynamics," Master's thesis, University of Glasgow, 2021, http://theses.gla.ac.uk/id/eprint/82702;

47. Qiao, G., Zhang, T., and Barakos, G., "Numerical simulation of distributed propulsion systems using CFD," *Aerospace Science and Technology*, 2024, pp. 109011. DOI: 10.1016/j.ast.2024.109011;

48. Menter, F.R., "Two-equation eddy-viscosity turbulence models for engineering applications," *AIAA journal*, Vol. 32, No. 8, 1994, pp. 1598–1605;

49. Qiao, Geng and San Martin, Emma and Barakos, George, Assessment of Synchrophasing for a Pair of Rotors in Close Proximity. Available at SSRN:

https://ssrn.com/abstract=4811595 or http://dx.doi.org/10.2139/ssrn.4811595;

50. Smith, D., Filippone, A., and Barakos, G., "Acoustic analysis of counterrotating open rotors with a locked blade row," *AIAA Journal*, Vol. 58, No. 10, 2020, pp. 4401–4414;
51. Kroll, N., Rossow, C. C., Becker, K. and Thiele, F., "MEGAFLOW-a numerical flow simulation system," 21st ICAS congress, Melbourne, Austrila, Sep. 1998, pp. 09–13;
52. Keßler, M., Frey, F., Letzgus, J., Ohrle, C., Thiemeier, J. and Krämer, E., "Progress in IAG's Rotorcraft Simulation Framework," *High Performance Computing in Science and Engineering, 20*, Springer International Publishing, 2021, pp. 331-341. ISBN: 978-3-030-80602-6;
53. Keßler, M., and Wagner, S., "Source-Time Dominant Aeroacoustics," *Computers & Fluids*, Vol. 33, 2004, pp. 791–800;
54. Jameson, A., "Time Dependent Calculations Using Multigrid, with Applications to Unsteady Flows Past Airfoils and Wings," AIAA 10th Computational Fluid Dynamics Conference, Honolulu, Hawaii, June 1991. DOI: 10.2514/6.1991-1596;
55. Borges, R., Carmona, M., Costa, B. and Don, W. S., "An Improved Weighted Essentially Non-Oscillatory Scheme for Hyperbolic Conservation Laws," *Journal of Computational Physics*, Vol. 227, (6), March 2008, pp. 3191-3211. DOI: 10.1016/j.jcp.2008.11.038;
56. De Gregorio, F., Visingardi, A., Iuso, G. An Experimental-Numerical Investigation of the Wake Structure of a Hovering Rotor by PIV Combined with a Γ_2 Vortex Detection Criterion, *Energies*. 2021, 14, 2613. https://doi.org/10.3390/en14092613.

10. CLASSIFICATION & COPYRIGHT